Cdh1 and *Pik3ca* Mutations Cooperate to Induce Immune-Related Invasive Lobular Carcinoma of the Breast

Yeji An[1,2,10], **Jessica R. Adams**#[1,10], **Daniel P. Hollern**#[3,10], **Anthony Zhao**#[4,5], **Stephen G. Chang**[4,5], **Miki S. Gams**[4,5], **Philip E.D. Chung**[6,7], **Xiaping He**[3], **Rhea Jangra**[1], **Juhi S. Shah**[1], **Joanna Yang**[1], **Lauren A. Beck**[1], **Nandini Raghuram**[1,2], **Katelyn J. Kozma**[1,2], **Amanda J. Loch**[1], **Wei Wang**[1], **Cheng Fan**[3], **Susan J. Done**[7,8,9], **Eldad Zacksenhaus**[6,7], **Cynthia J. Guidos**[4,5], **Charles M. Perou**[3,*], and **Sean E. Egan**[1,2,11,*]

[1]Program in Cell Biology, The Peter Gilgan Center for Research and Learning, The Hospital for Sick Children, Toronto, ON M5G-0A4, Canada

[2]Department of Molecular Genetics, University of Toronto, Toronto, ON, Canada

[3]Lineberger Comprehensive Cancer Center, Departments of Genetics and Pathology, University of North Carolina, Chapel Hill, NC 27599, USA

[4]Program in Developmental and Stem Cell Biology, The Peter Gilgan Center for Research and Learning, The Hospital for Sick Children, Toronto, ON M5G-0A4, Canada

[5]Department of Immunology, University of Toronto, Toronto, ON, Canada

[6]Division of Cell and Molecular Biology, Toronto General Research Institute, University Health Network, and Department of Medicine, University of Toronto, Toronto, ON, Canada

[7]Department of Laboratory Medicine and Pathobiology, University of Toronto, Toronto, ON, Canada

[8]Department of Medical Biophysics, University of Toronto, Toronto, ON, Canada

[9]The Campbell Family Institute for Breast Cancer Research at the Princess Margaret Cancer Centre and The Laboratory Medicine Program, University Health Network, Toronto, ON, Canada

[10]These authors contributed equally

[11]Lead Contact

# These authors contributed equally to this work.

*Correspondence: cperou@med.unc.edu (C.M.P.), segan@sickkids.ca (S.E.E.).

SUMMARY

CDH1 and *PIK3CA* are the two most frequently mutated genes in invasive lobular carcinoma (ILC) of the breast. Transcription profiling has identified molecular subtypes for ILC, one of which, immune-related (IR), is associated with gene expression linked to lymphocyte and macrophage infiltration. Here, we report that deletion of *Cdh1*, together with activation of *Pik3ca* in mammary epithelium of genetically modified mice, leads to formation of IR-ILC-like tumors with immune cell infiltration, as well as gene expression linked to T-regulatory (Treg) cell signaling and activation of targetable immune checkpoint pathways. Interestingly, these tumors show enhanced Rac1-and Yap-dependent transcription and signaling, as well as sensitivity to PI3K, Rac1, and Yap inhibitors in culture. Finally, high-dimensional immunophenotyping in control mouse mammary gland and IR-ILC tumors by mass cytometry shows dramatic alterations in myeloid and lymphoid populations associated with immune suppression and exhaustion, highlighting the potential for therapeutic intervention via immune checkpoint regulators.

Graphical Abstract
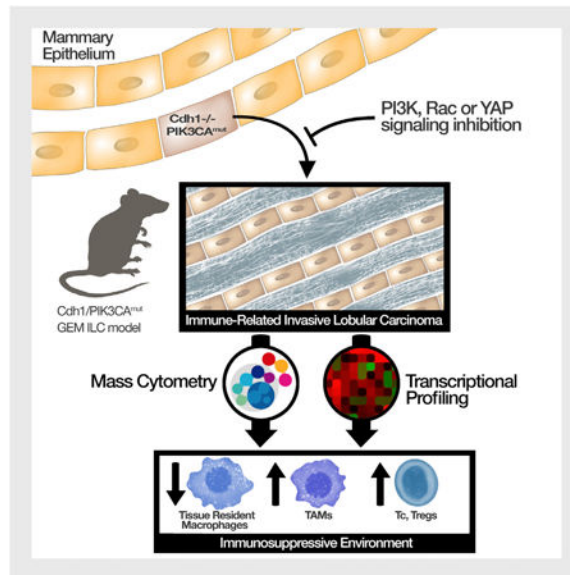
In Brief

An et al. describe the development and characterization of a mouse model for invasive lobular carcinoma (ILC) of the breast based on the two most mutated genes in human ILC. This model is analogous to immune-related ILC, shows myeloid and T cell alterations consistent with immune suppression and exhaustion, and represents a platform for therapeutics.

INTRODUCTION

Invasive lobular carcinoma (ILC) is the second most common histological type of breast cancer (BC) and most frequently diagnosed ''special type,'' accounting for approximately 10% of all breast tumors (McCart Reed et al., 2015; Weigelt et al., 2010b). Typical ILC shows a characteristic infiltrative pattern, with single-file rows of discohesive cells separated

by a collagen-rich matrix (Moinfar, 2007). Most lobular BCs are slow growing and low grade and express receptors for estrogen as well as progesterone. Consistent with these features, ILC patients have a relatively favorable 5-year survival rate. However, these tumors show local recurrence, exhibit diminished response to hormone and chemotherapy compared with invasive ductal carcinoma (IDC) (Metzger Filho et al., 2015; Marmor et al., 2017), and can recur as lethal tumors many years after treatment (Korhonen et al., 2013; Pestalozzi et al., 2008; Colleoni et al., 2016).

Transcriptional profiling has shown significant differences in gene expression between ILC and IDC (Weigelt et al., 2010a). More recently, this approach has led to the identification of ILC subtypes. Ciriello et al. (2015) found three subtypes: immune-related, reactive-like, and proliferative. Michaut et al. (2016) reported two: immune-related and hormone-related. The immune-related (IR) subtype identified in each case was defined by overexpression of transcripts coding for interleukins, chemokines, and cytokines, as well as by gene expression linked to lymphocyte and macrophage function (Desmedt et al., 2017). Comprehensive genomic analysis from both groups revealed a very high frequency of *CDH1* loss-of-function and *PIK3CA* gain-of-function mutations (Ciriello et al., 2015; Michaut et al., 2016).

A major challenge to development of effective new therapy against IR-ILC is the lack of an immune-competent model. Such models can be used to define therapeutic vulnerabilities, including tumor-specific signaling pathways or a significant, but exhausted, anti-tumor immune response. Jonkers and colleagues have described several mouse models for ILC. For example, deletion of *Cdh1* and *Tp53* in mammary epithelium leads to the development of pleomorphic ILC, an aggressive but relatively rare non-classical ILC subtype (Derksen et al., 2011). The same group reported that deletion of *Cdh1* and *Pten* in mammary epithelium leads to tumors with more classical ILC-like features (Boelens et al., 2016). Immune infiltration has not been described in this model, except under conditions linked to immunogenicity associated with Cas9 expression (Annunziato et al., 2016). In this study, we describe a genetically modified mouse model based on mutations in the two most commonly mutated genes from human ILC: *Cdh1* and *Pik3ca*. In doing so, we aim to identify previously unknown features of ILC that can be exploited for the development of novel therapeutics.

RESULTS

Homozygous Loss-of-Function *Cdh1* Mutations Cooperate with Activated Alleles of *Pik3ca* in Mammary Epithelial Transformation

As noted above, the two most common alterations in human ILC are *CDH1* loss-of-function mutations and activating gain-of-function mutations in *PIK3CA*. Indeed, approximately 50% of *CDH1* mutant tumors have activating mutations in *PIK3CA* (Ciriello et al., 2015; Michaut et al., 2016), suggesting that these gene mutations may well cooperate to transform mammary epithelial cells. To model ILC of this genotype, we bred mice with a Cre-conditional mutant allele of *Cdh1* ($Cdh1^{loxP/loxP}$) (Boussadia et al., 2002) to Cre-conditional transgenics for activated mouse *Pik3ca* ($R26\text{-}LSL\text{-}Pik3ca^{E545K}$ and $R26\text{-}LSL\text{-}Pik3ca^{H1047R}$) (Adams et al., 2011) and to mice with a mammary epithelial specific Wap-Cre transgene

(Wagner et al., 1997). These mice were then mated to activate Wap-Cre expression, which is strongly induced at pregnancy day 14 (Wagner et al., 1997). Parous $Cdh1^{loxP/loxP}$;$R26$-LSL-$Pik3ca^{E545K}$;Wap-Cre and $Cdh1^{loxP/loxP}$;$R26$-LSL-$Pik3ca^{H1047R}$;Wap-Cre female mice developed mammary tumors with a mean latency of 64.7 and 73.4 days, respectively. In contrast, parous $R26$-LSL-$Pik3ca^{E545K}$;Wap-Cre and $R26$-LSL-$Pik3ca^{H1047R}$;Wap-Cre females, without $Cdh1$ gene deletion, formed mammary tumors with a mean latency of 199.8 and 112.3 days, respectively (Figure 1A). $Cdh1^{loxP/loxP}$;Wap-Cre females developed hyperplastic lesions and small mammary tumors after Cre activation, but all regressed at weaning. These lesions were related to those that formed in $Cdh1^{loxP/loxP}$;$R26$-LSL-$Pik3ca^{mut}$;Wap-Cre cohorts (see below and Figures S2A and S2B). Control mice did not form tumors over an 18-month follow-up period (Figure 1A). The mean number of mammary tumors per female mouse increased from approximately 4.0 in $R26$-LSL-$Pik3ca^{E545K}$; Wap-Cre cohort mice to greater than 8.7 in $Cdh1^{loxP/loxP}$;$R26$-LSL-$Pik3ca^{E545K}$;Wap-Cre animals (p = 7.137 3 10 ^{10}), whereas the number of mammary tumors per mouse was not altered by $Cdh1$ deletion in $Pik3ca^{H1047R}$ mutant cohorts (approximately 7.5 mammary tumors formed in female mice from $R26$-LSL-$Pik3ca^{H1047R}$;Wap-Cre and $Cdh1^{loxP/loxP}$;$R26$-LSL-$Pik3ca^{H1047R}$ Wap-Cre cohorts) (data not shown).

For $Pik3ca^{H1047R}$ mice, we observed a sizable reduction in mammary tumor-free survival (MTFS) with deletion of $Cdh1$ (p = 1.02×10^{-11}). In contrast, for $Pik3ca^{E545K}$ mice, $Cdh1$ deletion did not significantly affect MTFS at 18 months (p = 0.264). However, at 150 and 250 days, deletion of $Cdh1$ had a dramatic effect on MTFS of $Pik3ca^{E5454K}$ cohort mice (p = 6.78×10^{-6} and p = 8.58×10^{-3}, respectively). This can be seen in Figure 1A, as MTFS curves for $Cdh1^{loxP/loxP}$;$R26$-LSL-$Pik3ca^{E545K}$;Wap-Cre and $R26$-LSL-$Pik3ca^{E545K}$;Wap-Cre cohorts cross just after 250 days. Importantly, these curves report the date on which mammary tumor burden for each animal required sacrifice, as opposed to the date on which tumors were first observed. Indeed, for $Cdh1^{loxP/loxP}$;$R26$-LSL-$Pik3ca^{E545K}$;Wap-Cre mice, mean average tumor growth (89.2 ± 15.9 days, from date of tumor observation until sacrifice) was slower than seen in $R26$-LSL-$Pik3ca^{E545K}$;Wap-Cre (25.8 ± 3.2 days) and $Cdh1^{loxP/loxP}$;$R26$-LSL-$Pik3ca^{H1047R}$;Wap-Cre mice (26.4 ± 1.5 days). In addition, box-and-whisker plot analysis of mammary tumor growth rate reveal more outliers (representing very slow growing tumors) in the $Cdh1$;$Pik3ca^{E545K}$ mutant cohort (data not shown). The very slow growing mammary tumors in $Cdh1^{loxP/loxP}$;$R26$-LSL-$Pik3ca^{E545K}$;Wap-Cre mice explains the long and shallow tail for MTFS seen on Figure 1A.

Next, mammary tumors from each cohort were analyzed by histology. The vast majority of lesions that formed in $Cdh1^{loxP/loxP}$;R26-LSL-$Pik3ca^{mut}$;Wap-Cre double-mutant mice were scirrhous tumors (Figures 1B and S1A). These are quite distinct from tumors that form in $Pik3ca$ single-mutant mice. The $Pik3ca^{E545K}$ single mutant induced mostly adenosquamous carcinomas (ASCs) (78%), with a number of other histotypes seen in a small percentage of tumors (Figures 1C and S1B). Forty-six percent of tumors in $Pik3ca^{H1047R}$;Wap-Cre transgenics were scirrhous tubular carcinomas, and 21% were ASCs. Other histologies were seen in a small percentage of cases (Figures 1C and S1B). Results from these control cohorts are consistent with a published report on transgenic models for E545K- and H1047R-induced mammary tumors (Meyer et al., 2013). Thus, both hotspot mutant alleles of $Pik3ca$ cooperate with $Cdh1$ loss-of-function mutations to induce ILC-like tumors in mice

(unpublished data and see below). Because $Cdh1^{loxP/loxP}$;R26-LSL-$Pik3ca^{H1047R}$;Wap-Cre model tumors were more aggressive, we focused on these for more comprehensive analysis. To this end, we tested for E-cadherin expression and PI3K activation and confirmed dramatically reduced E-cadherin accumulation as well as Akt activation in the H1047R mutant model (Figure S1C).

Cdh1/*Pik3ca* Double-Mutant Tumors Are Diffusely Infiltrative and Highly Related to Human ILC

Upon necropsy, it was immediately clear that tumors in $Cdh1^{loxP/loxP}$;R26-LSL-$Pik3ca^{H1047R}$;Wap-Cre mice were unlike those that form in models for IDC. Mammary lesions had irregular borders, which invaded mammary fat pads, musculature, and skin (Figures 2A and S2C; data not shown). They were so diffusely infiltrative that it was often difficult to determine where one tumor ended and another began. Indeed, tumors grew from one mammary gland into the next. Some tumors even crossed the midline, joining up on either side of the mouse, either around the back of the neck between anterior mammary fat pads on either side or across the lower abdomen, joining the most posterior fat pads into a contiguous tumor network (Figure 2B). Tumors that formed in *Cdh1;Pik3ca* double-mutant mice had less connective tissue than in human lobular BC. This is likely related to differences in stroma seen in the normal mammary gland of both species (McNally and Stein, 2017). Despite this, $Cdh1^{loxP/loxP}$;R26-LSL-$Pik3ca^{H1047R}$;Wap-Cre mammary tumors had many features in common with human ILC. For example, there were single-file rows of discohesive cells separated by fibrous tissue (Figure 2C), targetoid growth patterns (Figure 2D), and epithelial-like structures within most tumors (Figure S2D). Interestingly, tumorspheres from this model showed characteristic single-file outgrowth in three-dimensional (3D) culture (Figures S2E and S2F). These features are similar to what was reported in mammary tumors from $Cdh1^{loxP/loxP}$;$Pten^{loxP/loxP}$;Wap-Cre mice, a model for less common *CDH1*;*PTEN* double-mutant ILC (Boelens et al., 2016). Extensive collagen deposition was seen by Masson's trichrome staining (Figure 2E). By transmission electron microscopy, extracellular matrix fibers could be seen to separate individual rows of tumor cells in $Cdh1^{loxP/loxP}$;R26-LSL-$Pik3ca^{H1047R}$; Wap-Cre lesions (data not shown). Also, some tumor cells had apical membrane anomalies, with interdigitated microvilli at the cell surface as well as very small lumens separating adjacent cells or vesicles of apical membrane trapped within the cytoplasm (Figures 2F, S2G, and S2H; data not shown). These features have been seen in human ILC (Nesland et al., 1985) and are most likely attributable to alterations in membrane trafficking associated with loss of E-cadherin-dependent adherens junctions. Despite this, junctional complexes were evident in many tumor cells (Figure 2F). We next stained tumor sections with antibodies against receptors for estrogen (ERa) and progesterone (PR). Both receptors were expressed in double-mutant tumors (Figures 2G and 2H). These tumors expressed the luminal marker cytokeratin 8 (CK8) (Figure S2I). Surprisingly, some tumor cells, particularly those in peripheral regions, also or alternatively expressed basal cell cytokeratins (Figure S2J). As expected, tumor cells were negative for E-cadherin staining, although cytoplasmic p120 staining was apparent (Figure S2K). Smooth muscle actin was also detected, primarily in tumor stroma (Figure S2L).

A Model for IR ILC

Transcriptional profiling has been used to characterize mouse models of BC (Hollern and Andrechek, 2014; Pfefferle et al., 2013). To this end we used unsupervised hierarchical clustering to compare gene expression in mammary tumors from $Cdh1^{loxP/loxP}$;$R26$-LSL-$Pik3ca^{H1047R}$;Wap-Cre mice with mammary tumors from 27 distinct genetically engineered and mutant mouse (GEMM) strains, including models for ER$^+$, HER2$^+$, basal-like, and other triple-negative BCs (Pfefferle et al., 2013) (Figure S3). Gene expression profiles among $Cdh1^{loxP/loxP}$; R26-LSL-$Pik3ca^{H1047R}$ double-mutant tumors were highly correlated (centroid correlation > 0.9), and all ten assayed tumors clustered together without interruption by even a single tumor from any of the other models. Neighboring tumors within this cluster were from FVB, BALB/C, and SV129 SV/EV genetic backgrounds. Tumors with the greatest similarity to those from $Cdh1^{loxP/loxP}$;$R26$-LSL-$Pik3ca^{H1047R}$;Wap-Cre mice were from $Stat1^{-/-}$, MMTV-ATX, and $R26$-LSL-$Pik3ca^{H1047R}$;MMTV-Cre mice, all of which are ERα$^+$. This is not too surprising given that lobular tumors are typically ER$^+$, as is our model (see above). Unsupervised clustering highlighted four features of $Cdh1^{loxP/loxP}$;R26-LSL-$Pik3ca^{H1047R}$ tumors (blue blocks on the right-hand side of Figure S3A, expanded in Figure S3B; see also Table S1). The first block shows reduced expression of many genes associated with proliferation, including genes coding for Ki67, Mcm6, and cyclins. This finding is consistent with the relatively slow growth of these tumors, which is also seen in human ILC (Ciriello et al., 2015). Next, we saw low expression of $Cdh1$, as expected on the basis of its deletion in this model. Furthermore, gene sets 3 and 4 show elevated expression of mesenchymal and lymphocyte genes, respectively (see below). In agreement, gene set enrichment analysis (GSEA) revealed enrichment of signatures related to the mesenchymal differentiation and immune micro-environment (data not shown), where the former likely represents increased stroma seen in ILC (Dennison et al., 2016). Moreover, we observed enrichment of signaling pathway-specific signatures and lobular BC signatures.

Next, we used hierarchical clustering to test for a relationship between $Cdh1^{loxP/loxP}$;$R26$-LSL-$Pik3ca^{H1047R}$ mammary tumors and human BC. Given that PAM50 separates human BCs according to their intrinsic subtype, not necessarily according to their pathological subtype, we tested for relationships using genes that define lobular subtype tumors in humans (Ciriello et al., 2015) and those that define $Cdh1^{loxP/loxP}$;$R26$-LSL-$Pik3ca^{H1047R}$ tumors in mice (Table S1). As depicted in Figure 3A, this separated human luminal A tumors into two major clusters and also separated subtypes of human lobular BC as expected. Importantly, we observed co-clustering between human IR-ILC and murine mammary tumors from $Cdh1^{loxP/loxP}$;$R26$-LSL-$Pik3ca^{H1047R}$ mice. Given the similarity of these tumors, we used GSEA to investigate whether genes that define IR ILC were significantly enriched in $Cdh1^{loxP/loxP}$;$R26$-LSL-$Pik3ca^{H1047R}$ tumors. Indeed, a comparison of $Cdh1^{loxP/loxP}$; $R26$-LSL-$Pik3ca^{H1047R}$ tumors with all other mouse models revealed significant enrichment for high expression of genes that define IR ILC (Figure 3B), as well as individual genes and signatures that define immune cells (Figures S4A and S4B). Similarly, we interrogated co-clustered human IR ILC with genes that are highly expressed in $Cdh1^{loxP/loxP}$;$R26$-LSL-$Pik3ca^{H1047R}$ tumors and observed significant enrichment (Figure 3C).

A number of immune-cell specific gene signatures were highly expressed in IR-ILC and *Cdh1^loxP/loxP;R26-LSL-Pik3ca^H1047R* tumors (Figure 4A). In addition, many human luminal A ILC tumors, beyond those classified as immune related, had evidence of immune infiltration. By comparison, the majority of mouse models in our dataset showed much lower expression of immune signatures. Likewise, within the luminal A IDC pathology group, we observed high expression of immune signatures in only a minor subset of tumors. Among key common immune features, uniform elevation of signatures for immune checkpoints (CTLA4 and PD1) was shared by *Cdh1^loxP/loxP;R26-LSL-Pik3ca^H1047R* and the human IR ILC tumors, as were signatures for many T cell subsets (with the notable exception of TH2 T cells). Specific to *Cdh1^loxP/loxP;R26-LSL-Pik3ca^H1047R* tumors and human IR-ILC, we saw prominent elevation of the T-regulatory cell signature in nearly every sample. Importantly, we confirmed the presence of immune cells in *Cdh1^loxP/loxP;R26-LSL-Pik3ca^H1047R* tumors. Using IHC, we identified abundant CD3-postive staining at the tumor margins and more moderate staining within tumors (Figure S5A), a situation present in each of the tumors examined. Furthermore, we noted tertiary lymphoid structures, with CD3+ T cell and Btk+ B cell staining (Figures S5A and S5B), in some tumors. Together, these data indicate that immune infiltration is a prominent feature of ILC tumors shared by this new model. Moreover, the notable elevation of signatures associated with immune suppression, such as PD1, CTLA4, and T-regulatory cells, appears to be shared by *Cdh1^loxP/loxP;R26-LSL-Pik3ca^H1047R* tumors and human IR-ILC tumors, suggesting potential for these features as a therapeutic target.

We next looked for similarities between tumors in *Cdh1^loxP/loxP;R26-LSL-Pik3ca^H1047R* mice and IR-ILC beyond immune infiltration (Figure 4B). Overall, *Cdh1^loxP/loxP;R26-LSL-Pik3ca^H1047R* tumors and human IR-ILC tumors displaye remarkable consistency for upregulation of key signaling pathways, many of which mors and human IR-ILC tumors displayed remarkable consistency for upregulation of key signaling pathways, many of which were also highly expressed across luminal A ILC in general. Concordant with single-gene profiling, we saw low expression of signatures for cell cycle progression pathways in *Cdh1^loxP/loxP;R26-LSL-Pik3ca^H1047R* tumors and human ILC. As expected, pathway signatures for b-catenin and Pik3ca/PI3K were elevated in ILC tumors from both species. As seen in pleiomorphic lobular cancers, we detected elevation of HIF1a (Ercan et al., 2012) and Vegfa signaling. The most consistent relationship between all ILC tumors (mouse and human) was elevation of a signature for sonic hedgehog (Shh) signaling, consistent with the mesenchymal nature of these tumors (Maitah et al., 2011; Xu et al., 2012b), as well as elevation of a BC metastasis signature (Van't Veer et al., 2002). Among elevated pathways uniquely shared between *Cdh1^loxP/loxP;R26-LSL-Pik3ca^H1047R* tumors and human IR-ILC tumors were Rac1, YAP, Oct4, and Notch, many of which are related to high invasive potential of these lesions (Bailey et al., 2007; Lamar et al., 2012; Baugher et al., 2005; Chiou et al., 2010). Interestingly, a signature for tumor cell invasion was extremely high in *Cdh1^loxP/loxP;R26-LSL-Pik3ca^H1047R* tumors and was consistently elevated in coclustering human ILCs. Of note, these pathway and invasive signatures provide an important distinction between IR-ILC tumors, where despite sharing high expression of immune signatures, it is those IR-ILC tumors with invasive gene expression features that cluster with

our mouse model (Figure S5C). As a result, this mouse model mimics highly invasive, immune-infiltrated human ILCs, potentially by activation of similar cell signaling pathways.

Next, we compared our model with other recently described models for $Cdh1^{-/-};Pten^{-/-}$ ILC (Boelens et al., 2016) as well as for ILC induced by $Cdh1$ deletion together with oncogenic insertions associated with sleeping beauty transposon mobilization (Kas et al., 2017). Using preprocessing methods and COMBAT, we corrected for technical variance between these data and our dataset. Observing the intrinsic cluster (Figure 5A), domestic $p53/Brca1$-null tumors clustered with imported tumor data from the same model, squamous tumors tightly clustered with squamous tumors from the imported data, and our claudin-low tumors tightly clustered with spindle tumors from the imported data, demonstrating mediation of technical bias. As expected, $Cdh1^{loxP/loxP};R26\text{-}LSL\text{-}Pik3ca^{H1047R};Wap\text{-}Cre$ shared cluster with $Cdh1^{loxP/loxP};Pten^{loxP/loxP};Wap\text{-}Cre$ and tumors noted to be ILC subtype 1 from the ''sleeping beauty'' screen (SB-ILC1). Normal mammary gland samples were also present in this cluster, consistent with normal-like features of ILC.

To investigate how these models might be different, we used significance analysis of microarrays (SAM) to identify genes with differential regulation between our model and $Cdh1^{-/-};Pten^{-/-}$ tumors as well as between our model and SB-ILC1 (Figure S6A). From each comparison, a large number of gene expression differences were observed. To investigate changes unique to our model, significant genes from each comparison with $q = 0$ and fold change greater than 2 were identified (Figure S6B). Interestingly, upregulated genes in our model were associated with a number of invasive features such as MMP activity, collagen secretion, and microtubule dynamics (Figure S6C). In agreement, Mmp9, Mmp12, Mmp13, and a cancer invasiveness signature were all expressed significantly higher in $Cdh1^{loxP/loxP};R26\text{-}LSL\text{-}Pik3ca^{H1047R}$ tumors compared with other ILC models (Figure 5B). Likewise, Rac1, Yap, and Oct 4 pathway signatures were also significantly higher in $Cdh1^{loxP/loxP};R26\text{-}LSL\text{-}Pik3ca^{H1047R}$ tumors (Figure 5C). The SHH signature was more even between our model and other ILC models but still significantly higher compared with $Cdh1^{-/-};Pten^{-/-}$ tumors or SB-ILC2 tumors. To test for tumor cell dependence on altered signaling, we performed mitochondrial activity assays (MTT) on tumorsphere and control mammosphere cultures treated with inhibitors of PI3K (BKM120 and BYL719), Rac1 (NSC23766), or Yap1 (verteporfin). Indeed, tumorsphere cultures showed greater sensitivity to inhibitors of all three pathways at multiple concentrations (Figures 6A–6C). PI3K and Rac1 inhibitors cooperated in this regard (Figure 6D).

Upon testing immune cell signatures, similar expression patterns were observed between our model and the $Cdh1^{loxP/loxP};Pten^{loxP/loxP};Wap\text{-}Cre$ model (Figure 5D). However, macrophage signatures were significantly higher in $Cdh1^{loxP/loxP};R26\text{-}LSL\text{-}Pik3ca^{H1047R}$ tumors. As a whole, these comparisons suggest that although $Cdh1^{loxP/loxP};R26\text{-}LSL\text{-}Pik3ca^{H1047R}$ tumors are similar to other ILC models from a global gene expression perspective, key differences exist in terms of invasive potential, pathway activation, and immune cell composition.

Finally, we performed high-dimensional immunophenotyping by mass cytometry to identify phenotype and abundance of immune cell subsets in enzymatically dissociated mammary

glands (MGs) from control (CTRL) versus tumor-bearing mice. This technique uses an elemental mass spectrometer-coupled flow cytometer known as a CyTOF to analyze expression of single cells stained with 40 or more metal-tagged markers and can identify known and novel cell subsets when the data are analyzed using unsupervised computational approaches. We stained cell suspensions with 27–33 metal-tagged antibodies that included markers to identify epithelial cells, fibroblasts, and endothelial cells as well as several immune cell types and differentiation states (Table S2). As expected, the MG tumors contained a significantly higher proportion of epithelial (Epcam$^+$) relative to non-epithelial cells among CD45 non-hematopoietic cells (Figure S7A). MG cells from CTRL mice had slightly higher frequencies of CD45$^+$ cells, but the relative abundance of major immune cell lineages (T, B, myeloid, and natural killer [NK] cells) was not significantly different in CTRL versus tumor-bearing MG samples.

To determine whether immune cells infiltrating ILC tumor versus CTRL MG samples consisted of distinct sub-lineages and differentiation states, we performed unsupervised clustering of CD45$^+$ cells using Phenograph (Levine et al., 2015), a k-nearest neighbor algorithm, and used dimensionality reduction by t-distributed stochastic neighbor embedding (t-SNE) (Amir et al., 2013) to visualize the clusters (Figure 7A). B and NK cells mapped to three distinct clusters, which were not differentially abundant between CTRL and tumor MG samples (not shown). Among the nine CD11b$^+$ myeloid cell clusters, six were relatively low abundance and did not differ significantly between geno-types. These included CD11b^{lo} MHCII^{hi} CD24^{hi} dendritic cells, MHCII Ly6G$^+$ granulocytes, MHCII^{lo} Ly6C^{hi} monocytes and MHCII CD24^{hi} SiglecF$^+$ cells resembling alveolar macrophages (not shown) (Yu et al., 2016). Notably, however, tumor MG samples had significantly higher abundance of cluster 0, whereas CTRL samples had significantly higher abundance of clusters 3 and 5 within the myeloid population (Figure 7A). Cluster 0 showed uniquely high expression of CD11c (Itgax), previously identified to be expressed by tumor-associated but not normal mammary tissue macrophages (Franklin et al., 2014), as well as CD49F (Itga6). Plots of CD11c versus CD49F cells confirmed higher expression of both markers among tumor-associated CD11b$^+$ cells (Figure S7B). Thus, high-dimensional CyTOF analysis revealed that despite the similar overall abundance of myeloid cells in CTRL and tumor-bearing MGs, the ILC-like tumors in *Cdh$^{f/f}$; R26-Pik3ca$^{Mut+/-}$; Wap-Cre* mice promoted macrophages to adopt a unique differentiation state in the MG.

Phenograph analysis of CD3$^+$ TCRb$^+$ cells in MGs also revealed tumor-associated differences in T cell sub-lineages and differentiation states (Figure 6B). Tumor MG samples had significantly higher frequencies of clusters comprising the CD8β$^+$ cytotoxic and CD8β FoxP3$^+$ regulatory T cell lineages (Figures 7B and S7A). Interestingly, within the main CD8β$^+$, CD8β$^-$ FoxP3$^-$, and CD8β FoxP3$^+$ regulatory T subsets, significantly more cells expressed the immune ''exhaustion'' and inhibitory checkpoint marker PD1 in tumor MG samples (Figure 6B). Tumor-associated CD8β$^+$ and CD8β$^-$ FoxP3$^+$ T cells also had significantly higher PD1 expression, suggesting that they were activated (Figure 7B). Finally, PD1$^+$ regulatory T cells in tumor MG samples also expressed higher levels of the CD25 cytokine receptor (Figure S7C), providing further evidence that they were activated. Collectively these data suggest that development of MG tumors in this model is accompanied by generation of an immune suppressive micro-environment in which CD11c^{hi}

CD49F^{hi} macrophages as well as PD1^{hi} cytotoxic and regulatory T cells are more prevalent than in the normal MG.

DISCUSSION

The study of lobular BC has been hampered by a lack of cellular and animal models. Recently, Sflomos et al. (2016) used intra-ductal injection of human ILC into immune-compromised mice to generate xenograft models. This approach holds much promise, particularly for the study of hormone-related and reactive subtype disease (Ciriello et al., 2015; Michaut et al., 2016). In contrast, IR ILC must be studied in an immune-competent system. Genomic analysis has highlighted the importance of two common targets for mutation in lobular BC, *CDH1* and *PIK3CA*. For *CDH1*, mutations are loss of function and recessive. For *PIK3CA*, mutations are gain of function, are dominant, and occur mostly at one of two hotspots: H1047 in the kinase domain and E545 in the helical domain. Here we report that homozygous deletion of *Cdh1* cooperates with *Pik3ca*^{H1047R} to induce mouse mammary tumors with a dramatically reduced latency, in comparison with tumor formation induced by *Pik3ca*^{H1047R} alone (note that *Cdh1* deletion by itself does not induce mammary tumor formation). The situation with *Pik3ca*^{E545K} is more complicated. During the first ~8 months (250 days), *Pik3ca*^{E545K} cooperates with *Cdh1* deletion to induce mammary tumor formation at a higher rate. However, when followed for 18 months, the difference in MTFS between *Cdh1*$^{loxP/loxP}$; *Pik3ca*^{E545K};Wap-Cre and *Pik3ca*^{E545K};Wap-Cre cohorts disappeared. The exact reason for this difference between alleles is unclear, although *PIK3CA*^{E545K} mutants are mostly found in slow-growing luminal A breast tumors, whereas *PIK3CA*^{H1047R} mutations are common in both luminal A and luminal B (Cancer Genome Atlas Network, 2012). Perhaps this is related to inefficient activation of Akt by p110a^{E545K}, as opposed to p110a^{H1047R} (Meyer et al., 2013), or to the differential dependence of helical (E545K) versus kinase domain (H1047R) mutant proteins on Ras-GTP and tyrosine kinase signaling, respectively (Zhao and Vogt, 2010; Hao et al., 2013). Both types of *Cdh1*$^{loxP/loxP}$;*Pik3ca*^{mutant};Wap-Cre tumors are slow growing, but this feature is particularly striking in *Pik3ca*^{E545K} cohort mice. Thus, both hotspot alleles cooperate with *Cdh1* loss to initiate formation of slow growing luminal A ILC type mammary tumors.

Our mouse model for ILC is transcriptionally related to IR-ILC in humans, with clear evidence of leukocyte infiltration. Gene expression signatures for many different adaptive and innate immune cell types were evident in mouse and human lesions. Strikingly, immune cell infiltration was also associated with transcriptional evidence for immune suppression and/or immune cell exhaustion in both species. For example, a strong signature for Treg cells and for PD1- and CTLA4-based immune checkpoint activation was seen. Transcriptional profiling also revealed a number of gene expression programs and signaling pathways that show shared activation in *Cdh1*$^{loxP/loxP}$;*R26-LSL-Pik3ca*^{H1047R} tumors and human IR-ILC; this includes Rac1, Yap, Oct4, Hif1a, Shh, and Notch. In particular, results for Rac1, Yap, Oct4, and invasion signatures are noteworthy, as they further distinguish human tumors within the IR-ILC subtype, perhaps on invasive capacity. Also, mouse IR-ILC tumor cells show sensitivity to PI3K, Rac1, and Yap inhibitors. Given the similarity between our model and its human counterpart, its invasive capacity *in vivo* and *in vitro*, our model represents a unique counterpart of highly invasive IR-ILC at the level of tumor phenotype

and pathway activity. Interestingly, tumors in *Cdh1^loxP/loxP; Pten^loxP/loxP;Wap-Cre* mice also showed high-level expression of immune cell signatures, but not as high expression as our model for genes, pathways, and signatures associated with tumor invasiveness.

Using mass cytometry, we identified specific features of the immune system in our IR-ILC model. Most immune cell populations that could be identified in CTRL MGs appeared unchanged in mammary tumors, in terms of compartment size and marker expression. In contrast, striking abnormalities were identified in a few macrophage and lymphocyte compartments. For example, tissue resident macrophages were reduced in number, while a new CD11b$^+$, CD11c^{Hi} (Itgax), and CD49F (Itga6)^{Hi} macrophage compartment was present. Interestingly, tumor-associated macrophages (TAMs) in these lesions were MHC class II^{Hi}, suggesting that they were highly activated and distinct from those found in tumors that form in MMTV-polyoma MT mice (Franklin et al., 2014). Consistent with this, most CD11b$^+$ cells in our model were not VCAM^{Hi}, again distinct from those found in PyMT tumors (Franklin et al., 2014). Other studies have reported variable myeloid phenotypes in different mouse models of BC (Yu et al., 2016).

Marked differences were also seen between T cells in our IR-ILC-like tumors and those found in CTRL MGs. Tumors had more cytotoxic and regulatory T cells. These and other T cell populations showed evidence of previous activation (high PD1 and CD25 expression). One of these populations is likely related to CD4$^+$FoxP3$^-$ PD-1^{Hi} inhibitory T cells, which are thought to limit anti-tumor T cell responses (Zappasodi et al., 2018). Collectively these data suggest that development of MG tumors in this model is accompanied by generation of an immune suppressive micro-environment in which CD11c^{hi} CD49F^{hi} macro-phages as well as PD1^{hi} T cells are more prevalent than in the normal MG.

On the basis of these conserved features, the *Cdh1^loxP/loxP*; *R26-LSL-Pik3ca^H1047R*;*Wap-Cre* mouse will be an important preclinical model for testing a number of immune-based therapeutics. Mouse models for IDC of the breast, most prominently MMTV-PyMT, have been used to study roles for specific immune cell types in growth, progression, and dissemination (Dadi et al., 2016; Franklin et al., 2014). Going forward, however, it will be important to use models for specific breast tumor types, including well known molecular sub-types, to define exactly how the immune system functions in each. Indeed, immune phenotypes differ dramatically across models (Yu et al., 2016) and therefore likely differ in specific types of BC in humans. Ultimately, combination therapies can be developed with this model, on the basis of signaling defects (e.g., PI3K and Rac1), as well as on activation of effective immune clearance of tumor. Finally, this new model, which demonstrates significant invasive capacity, can be used as a platform for selection of therapy resistance and metastatic disease, as well as for identification of approaches to treat such disease.

STAR★METHODS

KEY RESOURCES TABLE

REAGENT or RESOURCE	SOURCE	IDENTIFIER
Antibodies		
Rabbit Anti-ERa (MC-20)	Santa Cruz Biotechnology	Sc-542; RRID: AB_631470
Rabbit Anti-PR (C-19)	Santa Cruz Biotechnology	Sc-538; RRID: AB_632263
Mouse Anti-cytokeratin 8 (Troma-1)	Developmental Studies Hybridoma Bank	Troma-1; RRID: AB_531826
Mouse Anti-cytokeratin 14 (LL002)	Abcam	Ab7800; RRID: AB_306091
Rabbit Anti- delta 1 Catenin (EPR357(2))	Abcam	Ab92514; RRID: AB_10565040
Mouse Anti-Smooth Muscle Actin (clone 1A4)	Millipore-Sigma	A2547 Sigma; RRID: AB_476701
Anti-CD3 antibody (CD3–12)	Abcam	Ab11089; RRID: AB_369097
Rabbit Anti-Btk (D3H5)	Cell Signaling Technology	CS8547; RRID: AB_10950506
AlexaFluor488 conjugated Donkey Anti-Mouse Ab	Thermo Fisher Scientific (Invitrogen)	A-21202; RRID: AB_141607
AlexaFluor488 conjugated Goat Anti-Rat Ab	Thermo Fisher Scientific (Invitrogen)	A-11006; RRID: AB_2534074
AlexaFluor594 conjugated Chicken Anti-Rabbit Ab	Thermo Fisher Scientific (Invitrogen)	A-21442; RRID: AB_2535860
Anti-Ly6C (HK1.4)	BioLegend	128002; RRID: AB_1134214
CD44 (IM7)	BioLegend	103002; RRID: AB_312953
CD4 (RM4–5)	BioLegend	100561; RRID: AB_2562762
SiglecF (E50–2440)	BD Biosciences	552125; RRID: AB_394340
Itgb7 (FIB504)	BioLegend	321218; RRID: AB_893553
CD11b (M1/70)	BioLegend	101202; RRID: AB_312785
CD19 (1D3)	Thermo Fisher	14-0193-82; RRID: AB_657650
CD24 (M1/69)	Thermo Fisher	14-0242-82; RRID: AB_467170
CD25 (3C7)	Thermo Fisher	16-0253-85; RRID: AB_2573074
CD3e (145–2C11)	BioLegend	100302; RRID: AB_312667
ICOS (7E.17G9)	BD Biosciences	552437; RRID: AB_394389
CD22 (Cy34.1)	This work	N/A
CD103 (M290)	BD Biosciences	553699; RRID: AB_394995
CD45 (30-G12)	This work	N/A
FOXP3 (FJK-16 s)	Thermo Fisher	14-5773-82; RRID: AB_467576
CXCR4 (L276F12)	Fluidigm	3159030B

REAGENT or RESOURCE	SOURCE	IDENTIFIER
Tbet (4B10)	BD Biosciences	624084 (Custom)
Vcam1 (429 (MVCAM.A))	BioLegend	105701; RRID: AB_313202
PD1 (RMP1–30)	Thermo Fisher	14–9981-85; RRID: AB_468656
CD8b (H35–17.2)	Thermo Fisher	14–0083-85; RRID: AB_657759
CD49F (eBioGoH3(GoH3))	Fluidigm	3164006B
CD31 (390)	Fluidigm	3165013B
Epcam (G8.8)	Fluidigm	3166014B
Ly6G (1A8)	BioLegend	127602; RRID: AB_1089180
CD8a (53–6.7)	This work	N/A
TCRb (H57–597)	BioLegend	109202; RRID: AB_313425
CD49b (HMa2)	Fluidigm	3170008B
CD11c (N418)	BioLegend	117302; RRID: AB_313771
Nrp1 (3DS304M)	Thermo Fisher	CUST03948
CD117 (2B8)	BD Biosciences	553352; RRID: AB_394803
MHC class II (M5/114.15.2)	BioLegend	107602; RRID: AB_313317
CD127 (A7R34)	BioLegend	135002; RRID: AB_1937287
RORgt (B2D)	Thermo Fisher	14–6981-82; RRID: AB_925759
Deposited Data		
Gene expression data from IR-ILC mouse model tumors	This work	GEO: GSE107432
Experimental Models: Cell Lines		
IR-ILC Tumorsphere cultures	This work	N/A
FVB Mammosphere cultures	This work	N/A
Experimental Models: Organisms/Strains		
Mouse: Cdh1 (B6.129-Cdh1^{tm2Kem}/J)	The Jackson Laboratory	Jax: 005319
Mouse: Wap-Cre (B6.Cg-Tg(Wap-cre)11738Mam/JKnwJ)	The Jackson Laboratory	Jax: 008735
Mouse: R26-LSL-Pik3ca^{H1047R} (FVB.129S6-Gt(ROSA)26Sor$^{tm1(Pik3ca*H1047R)Egan}$/J	The Jackson Laboratory	Jax: 016977
Mouse: R26-LSL-Pik3ca^{E545K} (FVB)	This work	N/A

REAGENT or RESOURCE	SOURCE	IDENTIFIER
Oligonucleotides		
Primer for genotyping Cdh1 loxP/+ mice: 5'-GGGTCTCACCGTAGTCCTCA-3' (oIMR9338)	https://www2.jax.org/protocolsdb/f?p=116:5:0::NO:5:P5_MASTER_PROTOCOL_ID,P5_JRS_CODE:28552,005319	Boussadia et al., 2002.
Primer for genotyping Cdh1 loxP/+ mice: 5'-GATCTTTGGGGAGAGCAGTCG-3' (oIMR9339)	https://www2.jax.org/protocolsdb/f?p=116:5:0::NO:5:P5_MASTER_PROTOCOL_ID,P5_JRS_CODE:28552,005319	Boussadia et al., 2002.
Primer for genotyping Wap-Cre mice: 5'-TAG AGC TGT GCC AGC CTC TTC-3' (oIMR0575) Transgene.	https://www2.jax.org/protocolsdb/f?p=116:5:0::NO:5:P5_MASTER_PROTOCOL_ID,P5_JRS_CODE:22331,003552	Wagner et al., 1997
Primer for genotyping Wap-Cre mice: 5'-GTG AAA CAG CAT TGC TGT CAC TT-3' (oIMR1085) Transgene.	https://www2.jax.org/protocolsdb/f?p=116:5:0::NO:5:P5_MASTER_PROTOCOL_ID,P5_JRS_CODE:22331,003552	Wagner et al., 1997
Primer for genotyping Wap-Cre mice: 5'-CAA ATG TTG CTT GTC TGG TG-3' (oIMR8744) Internal Positive Control Forward.	https://www2.jax.org/protocolsdb/f?p=116:5:0::NO:5:P5_MASTER_PROTOCOL_ID,P5_JRS_CODE:22331,003552	Wagner et al., 1997
Primer for genotyping Wap-Cre mice: 5'-GTC AGT CGA GTG CAC AGT TT-3' (oIMR8745) Internal Positive Control Reverse.	https://www2.jax.org/protocolsdb/f?p=116:5:0::NO:5:P5_MASTER_PROTOCOL_ID,P5_JRS_CODE:22331,003552	Wagner et al., 1997
Primer for genotyping *R26-LSL-Pik3ca^mut.* 5'-GCG AAG AGT TTG TCC TCA ACC-3' (oIMR8052) Mutant Reverse.	https://www2.jax.org/protocolsdb/f?p=116:5:0::NO:5:P5_MASTER_PROTOCOL_ID,P5_JRS_CODE:29915,016977	Adams et al., 2011
Primer for genotyping *R26-LSL-Pik3ca^mut.* 5'-AAA GTC GCT CTG AGT TGT TAT-3' (oIMR8545) Common.	https://www2.jax.org/protocolsdb/f?p=116:5:0::NO:5:P5_MASTER_PROTOCOL_ID,P5_JRS_CODE:29915,016977	Adams et al., 2011
Primer for genotyping *R26-LSL-Pik3ca^mut.* 5'-GGA GCG GGA GAA ATG GAT ATG-3' (oIMR8546) Reverse.	https://www2.jax.org/protocolsdb/f?p=116:5:0::NO:5:P5_MASTER_PROTOCOL_ID,P5_JRS_CODE:29915,016977	Adams et al., 2011
Software and Algorithms		
GSEA	https://genepattern.broadinstitute.org/gp/ pages/index.jsf	Subramanian et al., 2005
Cluster 3.0	http://bonsai.hgc.jp/~mdehoon/software/ cluster/software.htm	de Hoon et al., 2004
COMBAT	https://genepattern.broadinstitute.org/gp/ pages/index.jsf	Johnson et al., 2007
Java Tree View	http://bonsai.hgc.jp/~mdehoon/software/ cluster/software.htm	Saldanha, 2004
R Studio	https://www.rstudio.com/	NA

REAGENT or RESOURCE	SOURCE	IDENTIFIER
Significance Analysis of Microarrays	https://sourceforge.net/projects/mev-tm4/	Tusher et al., 2001
Cytoscape	http://www.cytoscape.org/	Shannon et al., 2003
STAR	https://github.com/alexdobin/STAR	Dobin et al., 2013
Salmon	https://combine-lab.github.io/salmon/	Patro et al., 2015
IGV	https://software.broadinstitute.org/software/igv/download	http://www.broadinstitute.org/igv.
Phenograph	github.com/jacob/PhenoGraph	Levine et al., 2015
viSNA	www.cytobank.org	Amir et al., 2013

CONTACT FOR REAGENTS AND RESOURCE SHARING

(Further information and requests for resources and software should be directed to and will be fulfilled by the Lead Contact, Sean Egan (segan@sickkids.ca).

EXPERIMENTAL MODEL AND SUBJECT DETAILS

Mouse model of IR-ILC Breast Cancer

Mice were housed at The Centre for Phenogenomics (TCP) in Toronto. Wap-Cre (JAX#008735) and *Cdh1$^{f/f}$* (JAX#005319) stains were obtained from Jackson labs. *R26-LSL-Pik3ca^{H1047R}* (JAX#016977) mice were previously generated in the Egan lab (Adams et al., 2011). *R26-LSL-Pik3ca^{E545K}* mice were generated in exactly the same way (Adams et al., 2011). Wap-Cre and *R26-LSL-Pik3ca^{mut}* stains were genotyped by PCR using primers published as indicated (Adams et al., 2011; Soriano, 1999). *Cdh1$^{loxP/loxP}$* stains were genotyped by PCR using the following primers, 5′-GGGTCTCACCGTAGTCCTCA-3′ and 5′-GATCTTTGGGAGAGCAG TCG-3′. Mouse mammary tumors were collected from humanely sacrificed mice once the tumors reached endpoint as defined by the Canadian Council on Animal Care (CCAC). Tumor assays were performed exclusively on female mice. These and all other animal experiments were performed with prior approval of the TCP Animal Care Committee and according to guidelines from the CCAC.

METHOD DETAILS

Tumor histology and immunohistochemistry

Approximately one half of each harvested tumor was fixed in 10% formalin and later embedded in paraffin by the pathology core at TCP. The remaining half was divided into smaller samples and either snap-frozen or stabilized in RNAlater (QIAGEN 76106). Paraffin sections (5 mm) were cut, mounted and stained with hematoxylin and eosin by the pathology department at TCP. Masson's trichrome staining was performed by the pathology department at the Hospital for Sick Children. Unstained paraffin sections were deparaffinized in xylene and rehydrated through an alcohol series before being subjected to antigen retrieval in a decloaking chamber (Biocare Medical; SetPoint1 = 125 C, 5 minutes; SetPoint2 = 90 C, 10 s), using epitope-retrieval solutions of either pH6 or pH9.

Immunohistochemistry

endogenous peroxidases were quenched in 3% H_2O_2 in methanol for 15 minutes (room temperature). VectaStain ABC kits (Vector Laboratories PK-6101, PK-4002, PK-6105) were used for subsequent steps. Slides were blocked for 1 hour. Primary antibodies were incubated overnight under moist conditions (4 C). Secondary antibodies were incubated for 1 hour at room temperature. 3,30 -Diaminobenzidine (DAB) substrate kit (Vector Laboratories SK-4100) was used for staining and slides were counterstained in hematoxylin for 10 s.

Immunofluorescence

slides were blocked for 1 hour (DakoCytomation X0909). Primary antibodies were incubated overnight under moist conditions (4 C). Secondary antibodies were incubated for 1 hour (room temperature). Slides were mounted with fluorescence mounting medium (DakoCytomation S3023) containing 40, 6-diamidino-2-phenylindole (DAPI).

Antibodies (used at recommended dilutions) are as follows

ERa (SantaCruz sc542), PR (SantaCruz sc538), Cytokeratin 8 (Troma-1; this antibody was developed by Philippe Brulet and Rolf Kemler, obtained from DSHB, developed under the auspices of the NICHD and maintained by The University of Iowa), Cytokeratin 14 (Abcam 7800), p120 d-catenin (Abcam ab92514), SMA (Sigma A2547), CD3 (Abcam 11089) and Btk (Cell Signaling Technology CS8547). AlexaFluor488 anti-mouse (Invitrogen A21202), AlexaFluor488 anti-rat (Invitrogen A11006) and AlexaFluor594 anti-rabbit (Invitrogen A21442).

Electron microscopy

To harvest high quality mammary tumor samples for electron microscopy (EM), heart perfusion was performed with a 0.05% glutar-aldehyde and 4% paraformaldehyde fixative solution on three $Cdh1^{loxP/loxP}$;$R26$-LSL-$Pik3ca^{H1047R}$;Wap-Cre mice. Fixed tumor samples were processed by the Nanoscale Biomedical Imaging Facility at the Hospital for Sick Children.

Tumorsphere assays

Mammary tumors were minced and digested in 1x collagenase/hyaluronidase (Stem Cell Technologies, #07912) for 4 hours at 37 C. Red blood cells (RBCs) were removed from digested tumors using RBC lysis solution (1:4 HBSS with 2% FBS:RBC Lysis Buffer, Sigma-Aldrich, #11814389001). After Trypsin-EDTA and dispase/DNase I treatments, cell suspension was passed through a 40 mm strainer (BD Falcon, #352340) to achieve single-cell suspension. Cells were incubated with a lineage antibody cocktail (anti-mouse TER-119, eBioscience, #14–5921; anti-mouse CD45, eBioscience, #14–0451; anti-mouse CD140a, eBioscience, #14–1401; anti-mouse CD31, eBioscience, #14–0311) for 30 minutes (4 C), then with Goat anti-rat IgG microbeads (Miltenyi Biotec, #120–000-290) for 15 minutes (4 C). Mammary epithelial (lineage depleted; lin⁻) cells (MECs) were isolated by using the autoMACS Pro Separator (Miltenyi Biotec). Cells were seeded at four different densities (1.0 3 10^5, 2.5 3 10^5, 5.0 3 10^5 and 7.5 3 10^5) onto ultra low attachment 6-well plates (Corning Costar, Fisher Scientific, #07–200-601) in MEC media (Advanced DMEM/F12, 2% FBS, 1% penicillin/streptomycin, EGF 10ng/mL, bFGF 10ng/mL, Heparin 4ng/mL, 5 mM ROCK inhibitor and 0.5 mM GSK3 inhibitor). Tumor-spheres were fed every other day and passaged every 3 days.

For inhibitor experiments (Figure 6), cell suspensions were generated using the same digestion and lineage depletion protocol described above. These cells were cultured for a few days before being trypsinized and replated at 2.0 3 10^4 cells/well on ultra low attachment 96-well plates (Corning Costar, Fisher Scientific 07–200-603) in MEC media. Different concentrations of the following inhibitors were added the next day: BKM120

dissolved in DMSO, BYL719 dissolved in DMSO, Verteporfin dissolved in DMSO (TOCRIS 5305) and NSC23766 dissolved in ddH$_2$O (Millipore Sigma 553502). Cells were exposed to the inhibitors for 48h before being incubated with MTT (0.2mg/mL) for 3h. Formazan products were dissolved in DMSO and plates read at 570nm using Molecular Devices VersaMax 190. Each plate was read twice, then both readings were averaged and corrected by subtracting absorbance readings from DMSO blanks. Viability percentages were calculated using the following equation: (corrected treated well)/(average of corrected CTRL wells) $\times$ 100.

Imaging

Histology and immunohistochemistry images were captured with an AxioCam HRm digital camera (Zeiss Axioskop) by using AxioVision (release 4.6.3) software. Immunofluorescence images were captured with a Hamamatsu C9100–13 EM-CCD camera (Quorum spinning disk confocal, Zeiss AxioVert 200M) by using Perkin Elmer Volocity software. EM images were captured on a Gatan Orius digital camera (FEI Tecnai 20 transition electron microscope) using Digital Micrograph software. Tumorsphere images were captured with a Leica DMI 6000 B microscope by using Leica Application Suite Advanced Fluorescence (release 3.2.0.96.52) software.

RNA extraction

Tumors frozen in RNAlater (QIAGEN 76106) were thawed and homogenized by QIAGEN TissueRupter (QIAGEN 9001271). RNA was extracted using a QIAGEN RNeasy mini kit (QIAGEN 74104). RNA was quantified by Nanodrop spectrophotometer and quality for microarray determined using an Agilent Bioanalyzer.

Gene Expression Analysis

Total RNA was labeled with cyanine-5 (Cy5) dye for tumor samples and cyanine-3 (Cy3) dye for mouse reference samples (Hersch-kowitz et al., 2007) using the Agilent Low RNA Input Fluorescent Linear Amplification Kit. For both mouse reference RNA and tumor RNA, 2ug of labeled RNA was co-hybridized overnight to Agilent microarrays (platform G4862A). This new gene expression data was deposited on the UNC Microarray Database (UMD). The gene expression data was extracted with other published data for mouse mammary tumor models (Pfefferle et al., 2013) from the UMD; please see Gene Expression Omnibus accession numbers GSE3165, GSE8516, GSE9343, GSE14457, GSE15263, GSE17916, GSE27101 and GSE42640 for data associated with Pfefferle et al. (Pfefferle et al., 2013). Gene expression was calculated as log2 Cy5/Cy3 ratios, keeping only probes with Lowess normalized intensity values greater than 10 in both Cy5 and Cy3 channels and keeping probes with data on greater than 70% of the microarrays (in the context of the entire dataset). The entire dataset was then median centered across genes using Cluster 3.0 (de Hoon et al., 2004) and missing values were imputed using K-means nearest neighbor imputation. Unsupervised hierarchical clustering of the mouse dataset was done using Cluster 3.0 using a gene filtering criteria based on standard deviation (SD > 1.0). Clustering was done using the correlation similarity metric and centroid linkage. Clustering results were visualized in Java Tree View (Saldanha, 2004). Fold change analysis was done using Significance Analysis of Microarrays (Tusher et al., 2001). Gene expression signature scores

were calculated as the median expression of the signature according to previously published methods (Fan et al., 2011). Gene-set enrichment analysis (Subramanian et al., 2005) (GSEA) was done using the Broad Institute Gene Pattern server (Reich et al., 2006) and GSEA results were visualized in Cytoscape (Shannon et al., 2003) using protocol from the Bader lab (http://www.baderlab.org/Software/ EnrichmentMap/Tutorial) (Merico et al., 2011).

For combined analysis of mouse and human tumors, mouse Entrez gene ids were mapped to their corresponding human gene symbol. The human tumor dataset was the TCGA Breast Cancer 1198 dataset, with IDC from all major subtypes and ILC samples (Ciriello et al., 2015). For mediation of platform biases (aka-batch effects), each mouse and human dataset was first independently normalized, log2 transformed, and imputed. Next, each dataset was independently median centered across genes, followed by sample standardization. Finally, the mouse and human datasets were combined by COMBAT (Johnson et al., 2007). For cluster analysis, genes were filtered to previously published signature genes for defining lobular subtypes (Ciriello et al., 2015) as well as the signature genes that define the $Cdh1^{loxP/loxP}$;$R26\text{-}LSL\text{-}Pik3ca^{H1047R}$ tumors (the mouse signature list combined SAM results from both comparisons of $Cdh1^{loxP/loxP}$;$R26\text{-}LSL\text{-}Pik3ca^{H1047R}$ tumors to other $Pik3ca^{H1047R}$ induced tumors and to all other mouse models in the dataset). Again, clustering relied upon Cluster 3.0 using the correlation similarity metric and centroid linkage. The clustering results were visualized and extracted using Java Tree View (Saldanha, 2004).

For comparative analysis to existing models of ILC, the fastQ files (single-end read samples only) were imported from the European Nucleotide Archive (PRJEB14134 and PRJEB14147). Alignment was conducted using STAR (Dobin et al., 2013) and quantification of aligned reads were achieved using SALMON (Patro et al., 2015). Sample identities were not shared for RNA-seq data PRJEB147 and thus IGV was used to view BAM-files and unblind data genotypes. Preprocessing of RNA-seq data included upper quartile normalization and removal of genes with an average less than 10 across the entire RNA-seq dataset. Next, the data was Log2 transformed, filtered to genes present across 70% of the data, and with missing values imputed. Next, the imported data and our domestic dataset were independently centered across genes, followed by sample standardization. Batch effects were then removed using COMBAT.

MASS CYTOMETRY METHODS

Cell Staining for Mass Cytometry

Dissected MG tissue from 12–24-week old CTRL or tumor-bearing mice (N = 4/group) was enzymatically digested to release single cells (Xu et al., 2012a). Fc receptors were blocked by treating cell suspensions (1–2×10^6 cells/mouse) with the 2.4G2 anti-FcRII/ FcRIII antibody in staining media (SM: phosphate-buffered saline (PBS) containing 1% bovine serum albumin). Cells were then stained for 30' at room temperature with pre-determined optimal concentrations of metal-tagged antibodies specific for cell surface markers diluted in SM. Cells were then washed in SM, pelleted (300 × g, 5′), and resuspended in SM containing 10 mM ^{195}Cisplatin (BioVision Inc., USA) to stain dead cells. After 3′, cells were washed again and then immediately fixed and permeabilized with Transcription Factor

buffer (BD BioSciences, San Jose CA) according to the manufacturer's instructions. After washing, cells were stained with transcription factor antibodies and then washed a final time before re-suspending in PBS containing 0.3% saponin, 1.6% formaldehyde, and 0.05 mM $^{191/193}$ Iridium to stain nuclear DNA for up to 48h at 4°C. Cells were then washed and re-suspended in deionized water at $2\text{--}5\times10^5$/ml prior to adding to 5-element EQ normalization beads (Fluidigm, Markham ON Canada) and running on a Helios CyTOF according to Fluidigm's protocols. The Helios software was used for pre-processing to generate and normalize FCS 3.0 datafiles.

Metal-tagged Antibodies

Purified carrier-free antibodies were purchased from BD Biosciences, BioLegend or Thermo Fisher and metal tagged using Fluidigm Maxpar Metal Conjugation Kits according to the manufacturer's instructions. The only exception was Ly6C, which was tagged using the MaxPar chemistry to natural abundance Indium(III) chloride (95.6% atomic mass 115) purchased from Sigma. One experiment (N = 3/group) was performed with the 33-marker panel shown in Table S1, and a second (N = 1/group) was with a similar panel of 27 markers.

CyTOF Data Analysis

FCS files were uploaded into Cytobank (Santa Clara, CA) and each parameter was scaled using the Arcsinh transformation. Each datafile was manually pregated to remove EQ beads, dead cells, debris and aggregates and to identify CD45$^+$ hematopoietic cells. FCS datafiles containing 11,198 CD45$^+$ live single cells from each sample were exported for clustering using the open source Phenograph algorithm (github.com/jacob/PhenoGraph)(Levine et al., 2015). Clustering was performed ($k = 30$, Arcsinh scale argument = 5) on 6 MG samples (3 CTRL and 3 Tumor) using the following 27 markers: Ly6C, CD44, SiglecF, Itgb7, CD11b, CD24, CD25, CD3e, Icos, CD22, CD103, CD45, FoxP3, CXCR4, Tbet, PD1, CD8b, CD49F, Ly6G, TCRβ, CD49b, CD11c, Nrp1, CD117, MHCII, CD127 and RORγt. The R package 'flowCore' was used to create new FCS files that included the Phenograph cluster IDs, which were then uploaded to Cytobank where t-SNE dimensionality reduction was performed (iterations = 2000, perplexity = 30, theta = 0.5) using the clustering markers. The Phenograph cluster IDs were also included to enhance visualization of the Phenograph clusters in the t-SNE embedding (Amir et al., 2013).

DATA AND SOFTWARE AVAILABILITY

Gene expression data from IR-ILC mouse model tumors is publically available through GEO using accession number GSE107432.

QUANITIFICATION AND STATISTICAL ANALYSIS

All statistical analysis for Kaplan-Meier (KM) survival curves was performed in R (http://www.r-project.org/). KM survival curves were generated using the ''survival'' library and the ''survfit'' function. Survival statistics were calculated as non-parametric log rank p values for censored survival data using the ''survdiff'' function. Censored data, represented

by ''j'' on KM survival curves, indicates the removal of a mouse from the study before end point. Mice were censored in the overall survival curves due to air exposure, drowning or use as a CTRL. In the tumor-free survival curves, mice were censored due to non-mammary tumor end points or deaths. Further details, including number of animals on tumor watch (n) are available within Figure 1. Statistical analysis for Figure 3 was performed using GSEA and the gene pattern server. Details are provided within the figure legend. For Figure 5, statistics were performed in Graphpad Prism, using an unpaired t test and two-tailed p value. Details are provided in the figure legend. Statistical analysis for inhibitor assays with individual drugs (Figure 6A, B, C) was performed using the one-way ANOVA function in GraphPad Prism 6. Tukey's multiple comparison test was done to calculate statistical differences between treatment and CTRL groups. Statistical analysis for the PI3K + Rac1 inhibitor assay (Figure 6D) was performed using the two-way ANOVA function in GraphPad Prism 6. Sidak's multiple comparison test was done to determine statistical differences between treatment and CTRL groups. Bar graphs (Figure 6A, B, C) and line graph (Figure 6D) show the mean % of viable cells in each well and the vertical lines show standard deviation. Further details are available within the figure legend. For Mass Cytometry, statistical significance of differential subset abundance was per-formed using multiple t tests in Prism 7. The two-stage step up method of Benjamini, Krieger and Yekutieli was used to correct for multiple testing (Benjamini et al., 2006). The number of tumor or CTRL MG samples (n) analyzed is provided within the Mass Cytometry Methods section.

Supplementary Material

Refer to Web version on PubMed Central for supplementary material.

ACKNOWLEDGMENTS

REFERENCES

Adams JR, Xu K, Liu JC, Agamez NM, Loch AJ, Wong RG, Wang W, Wright KL, Lane TF, Zacksenhaus E, and Egan SE (2011). Cooperation between *Pik3ca* and p53 mutations in mouse mammary tumor formation. Cancer Res 71, 2706–2717. [PubMed: 21324922]

Amir AD, Davis KL, Tadmor MD, Simonds EF, Levine JH, Bendall SC, Shenfeld DK, Krishnaswamy S, Nolan GP, and Pe'er D (2013). viSNE enables visualization of high dimensional single-cell data and reveals phenotypic heterogeneity of leukemia. Nat. Biotechnol 31, 545–552. [PubMed: 23685480]

Annunziato S, Kas SM, Nethe M, Yucel H, Del Bravo J, Pritchard C, Bin Ali R, van Gerwen B, Siteur B, Drenth AP, et al. (2016). Modeling invasive lobular breast carcinoma by CRISPR/Cas9-mediated somatic genome editing of the mammary gland. Genes Dev 30, 1470–1480. [PubMed: 27340177]

Bailey JM, Singh PK, and Hollingsworth MA (2007). Cancer metastasis facilitated by developmental pathways: Sonic hedgehog, Notch, and bone morphogenic proteins. J. Cell. Biochem 102, 829–839. [PubMed: 17914743]

Baugher PJ, Krishnamoorthy L, Price JE, and Dharmawardhane SF (2005). Rac1 and Rac3 isoform activation is involved in the invasive and metastatic phenotype of human breast cancer cells. Breast Cancer Res 7, R965–R974. [PubMed: 16280046]

Benjamini Y, Krieger AM, and Yekutieli D (2006). Adaptive linear step-up procedures that control the false discovery rate. Biometrika 93, 491–507.

Boelens MC, Nethe M, Klarenbeek S, de Ruiter JR, Schut E, Bonzanni N, Zeeman AL, Wientjens E, van der Burg E, Wessels L, et al. (2016). PTEN loss in E-cadherin-deficient mouse mammary epithelial cells rescues apoptosis and results in development of classical invasive lobular carcinoma. Cell Rep 16, 2087–2101. [PubMed: 27524621]

Boussadia O, Kutsch S, Hierholzer A, Delmas V, and Kemler R (2002). E-cadherin is a survival factor for the lactating mouse mammary gland. Mech. Dev 115, 53–62. [PubMed: 12049767]

Cancer Genome Atlas Network (2012). Comprehensive molecular portraits of human breast tumours. Nature 490, 61–70. [PubMed: 23000897]

Chiou S-H, Wang M-L, Chou Y-T, Chen C-J, Hong C-F, Hsieh W-J, Chang H-T, Chen Y-S, Lin T-W, Hsu H-S, and Wu CW (2010). Coexpression of Oct4 and Nanog enhances malignancy in lung adenocarcinoma by inducing cancer stem cell-like properties and epithelial-mesenchymal transdifferentiation. Cancer Res 70, 10433–10444. [PubMed: 21159654]

Ciriello G, Gatza ML, Beck AH, Wilkerson MD, Rhie SK, Pastore A, Zhang H, McLellan M, Yau C, Kandoth C, et al.; TCGA Research Network (2015). Comprehensive molecular portraits of invasive lobular breast cancer. Cell 163, 506–519. [PubMed: 26451490]

Colleoni M, Sun Z, Price KN, Karlsson P, Forbes JF, Thurlimann B, Gianni L, Castiglione M, Gelber RD, Coates AS, and Goldhirsch A (2016). Annual hazard rates of recurrence for breast cancer during 24 years of follow-up: results from the International Breast Cancer Study Group Trials I to V. J. Clin. Oncol 34, 927–935. [PubMed: 26786933]

Dadi S, Chhangawala S, Whitlock BM, Franklin RA, Luo CT, Oh SA, Toure A, Pritykin Y, Huse M, Leslie CS, and Li MO (2016). Cancer Immunosurveillance by tissue-resident innate lymphoid cells and innate-like T cells. Cell 164, 365–377. [PubMed: 26806130]

de Hoon MJ, Imoto S, Nolan J, and Miyano S (2004). Open source clustering software. Bioinformatics 20, 1453–1454. [PubMed: 14871861]

Dennison JB, Shahmoradgoli M, Liu W, Ju Z, Meric-Bernstam F, Perou CM, Sahin AA, Welm A, Oesterreich S, Sikora MJ, et al. (2016). High intratumoral stromal content defines reactive breast cancer as a low-risk breast cancer subtype. Clin. Cancer Res 22, 5068–5078. [PubMed: 27172895]

Derksen PW, Braumuller TM, van der Burg E, Hornsveld M, Mesman E, Wesseling J, Krimpenfort P, and Jonkers J (2011). Mammary-specific inactivation of E-cadherin and p53 impairs functional gland development and leads to pleomorphic invasive lobular carcinoma in mice. Dis. Model. Mech 4, 347–358. [PubMed: 21282721]

Desmedt C, Zoppoli G, Sotiriou C, and Salgado R (2017). Transcriptomic and genomic features of invasive lobular breast cancer. Semin. Cancer Biol 44, 98–105. [PubMed: 28400203]

Dobin A, Davis CA, Schlesinger F, Drenkow J, Zaleski C, Jha S, Batut P, Chaisson M, and Gingeras TR (2013). STAR: ultrafast universal RNA-seq aligner. Bioinformatics 29, 15–21. [PubMed: 23104886]

Ercan C, Vermeulen JF, Hoefnagel L, Bult P, van der Groep P, van der Wall E, and van Diest PJ (2012). HIF-1a and NOTCH signaling in ductal and lobular carcinomas of the breast. Cell Oncol. (Dordr.) 35, 435–442. [PubMed: 23008060]

Fan C, Prat A, Parker JS, Liu Y, Carey LA, Troester MA, and Perou CM (2011). Building prognostic models for breast cancer patients using clinical variables and hundreds of gene expression signatures. BMC Med. Genomics 4, 3. [PubMed: 21214954]

Franklin RA, Liao W, Sarkar A, Kim MV, Bivona MR, Liu K, Pamer EG, and Li MO (2014). The cellular and molecular origin of tumor-associated macrophages. Science 344, 921–925. [PubMed: 24812208]

Hao Y, Wang C, Cao B, Hirsch BM, Song J, Markowitz SD, Ewing RM, Sedwick D, Liu L, Zheng W, and Wang Z (2013). Gain of interaction with IRS1 by p110a-helical domain mutants is crucial for their oncogenic functions. Cancer Cell 23, 583–593. [PubMed: 23643389]

Herschkowitz JI, Simin K, Weigman VJ, Mikaelian I, Usary J, Hu Z, Rasmussen KE, Jones LP, Assefnia S, Chandrasekharan S, et al. (2007). Identification of conserved gene expression features between murine mammary carcinoma models and human breast tumors. Genome Biol 8, R76. [PubMed: 17493263]

Hollern DP, and Andrechek ER (2014). A genomic analysis of mouse models of breast cancer reveals molecular features of mouse models and relationships to human breast cancer. Breast Cancer Res 16, R59. [PubMed: 25069779]

Johnson WE, Li C, and Rabinovic A (2007). Adjusting batch effects in microarray expression data using empirical Bayes methods. Biostatistics 8, 118–127. [PubMed: 16632515]

Kas SM, de Ruiter JR, Schipper K, Annunziato S, Schut E, Klarenbeek S, Drenth AP, van der Burg E, Klijn C, Ten Hoeve JJ, et al. (2017). Insertional mutagenesis identifies drivers of a novel oncogenic pathway in invasive lobular breast carcinoma. Nat. Genet 49, 1219–1230. [PubMed: 28650484]

Korhonen T, Kuukasjarvi T, Huhtala H, Alarmo EL, Holli K, Kallioniemi A, and Pylkkanen L (2013). The impact of lobular and ductal breast cancer histology on the metastatic behavior and long term survival of breast cancer patients. Breast 22, 1119–1124. [PubMed: 23863867]

Lamar JM, Stern P, Liu H, Schindler JW, Jiang Z-G, and Hynes RO (2012). The Hippo pathway target, YAP, promotes metastasis through its TEAD-interaction domain. Proc. Natl. Acad. Sci. USA 109, E2441–E2450. [PubMed: 22891335]

Levine JH, Simonds EF, Bendall SC, Davis KL, Amir AD, Tadmor MD, Litvin O, Fienberg HG, Jager A, Zunder ER, et al. (2015). Data-driven phenotypic dissection of AML reveals progenitor-like cells that correlate with prognosis. Cell 162, 184–197. [PubMed: 26095251]

Liberzon A, Subramanian A, Pinchback R, Thorvaldsdottir H, Tamayo P, and Mesirov JP (2011). Molecular signatures database (MSigDB) 3.0. Bioinformatics 27, 1739–1740. [PubMed: 21546393]

Maitah MY, Ali S, Ahmad A, Gadgeel S, and Sarkar FH (2011). Up-regulation of sonic hedgehog contributes to TGF-b1-induced epithelial to mesenchymal transition in NSCLC cells. PLoS ONE 6, e16068. [PubMed: 21249152]

Marmor S, Hui JYC, Huang JL, Kizy S, Beckwith H, Blaes AH, Rueth NM, and Tuttle TM (2017). Relative effectiveness of adjuvant chemotherapy for invasive lobular compared with invasive ductal carcinoma of the breast. Cancer 123, 3015–3021. [PubMed: 28382636]

McCart Reed AE, Kutasovic JR, Lakhani SR, and Simpson PT (2015). Invasive lobular carcinoma of the breast: morphology, biomarkers and 'omics. Breast Cancer Res 17, 12. [PubMed: 25849106]

McNally S, and Stein T (2017). Overview of mammary gland development: a comparison of mouse and human. Methods Mol. Biol 1501, 1–17. [PubMed: 27796946]

Merico D, Isserlin R, and Bader GD (2011). Visualizing gene-set enrichment results using the Cytoscape plug-in enrichment map. Methods Mol. Biol 781, 257–277. [PubMed: 21877285]

Metzger Filho O, Giobbie-Hurder A, Mallon E, Gusterson B, Viale G, Winer EP, Thurlimann B, Gelber RD, Colleoni M, Ejlertsen B, et al. (2015). Relative effectiveness of letrozole compared with tamoxifen for patients with lobular carcinoma in the BIG 1–98 trial. J. Clin. Oncol 33, 2772–2779. [PubMed: 26215945]

Meyer DS, Koren S, Leroy C, Brinkhaus H, Muller U, Klebba I, Muller M, Cardiff RD, and Bentires-Alj M (2013). Expression of *PIK3CA* mutant E545K in the mammary gland induces heterogeneous tumors but is less potent than mutant H1047R. Oncogenesis 2, e74. [PubMed: 24080956]

Michaut M, Chin SF, Majewski I, Severson TM, Bismeijer T, de Koning L, Peeters JK, Schouten PC, Rueda OM, Bosma AJ, et al. (2016). Integration of genomic, transcriptomic and proteomic data identifies two biologically distinct subtypes of invasive lobular breast cancer. Sci. Rep 6, 18517. [PubMed: 26729235]

Moinfar F (2007). Essentials of Diagnostic Breast Pathology: A Practical Approach (Berlin: Springer-Verlag).

Nesland JM, Holm R, and Johannessen JV (1985). Ultrastructural and immunohistochemical features of lobular carcinoma of the breast. J. Pathol 145, 39–52. [PubMed: 2578561]

Patro R, Duggal G, and Kingsford C (2015). Salmon: accurate, versatile and ultrafast quantification from RNA-seq data using lightweight-alignment. bio-Rxiv https://doi.org/10.1101/021592.

Pestalozzi BC, Zahrieh D, Mallon E, Gusterson BA, Price KN, Gelber RD, Holmberg SB, Lindtner J, Snyder R, Thurlimann B, et al.; International Breast Cancer Study Group (2008). Distinct clinical and prognostic features of infiltrating lobular carcinoma of the breast: combined results of 15 International Breast Cancer Study Group clinical trials. J. Clin. Oncol 26, 3006–3014. [PubMed: 18458044]

Pfefferle AD, Herschkowitz JI, Usary J, Harrell JC, Spike BT, Adams JR, Torres-Arzayus MI, Brown M, Egan SE, Wahl GM, et al. (2013). Transcriptomic classification of genetically engineered mouse models of breast cancer identifies human subtype counterparts. Genome Biol 14, R125. [PubMed: 24220145]

Reich M, Liefeld T, Gould J, Lerner J, Tamayo P, and Mesirov JP (2006). GenePattern 2.0. Nat. Genet 38, 500–501. [PubMed: 16642009]

Saldanha AJ (2004). Java Treeview—extensible visualization of microarray data. Bioinformatics 20, 3246–3248. [PubMed: 15180930]

Sflomos G, Dormoy V, Metsalu T, Jeitziner R, Battista L, Scabia V, Raffoul W, Delaloye JF, Treboux A, Fiche M, et al. (2016). A preclinical model for ERa-positive breast cancer points to the epithelial microenvironment as determinant of luminal phenotype and hormone response. Cancer Cell 29, 407–422. [PubMed: 26947176]

Shannon P, Markiel A, Ozier O, Baliga NS, Wang JT, Ramage D, Amin N, Schwikowski B, and Ideker T (2003). Cytoscape: a software environment for integrated models of biomolecular interaction networks. Genome Res 13, 2498–2504. [PubMed: 14597658]

Soriano P (1999). Generalized lacZ expression with the ROSA26 Cre reporter strain. Nat. Genet 21, 70–71. [PubMed: 9916792]

Subramanian A, Tamayo P, Mootha VK, Mukherjee S, Ebert BL, Gillette MA, Paulovich A, Pomeroy SL, Golub TR, Lander ES, and Mesirov JP (2005). Gene set enrichment analysis: a knowledge-based approach for interpreting genome-wide expression profiles. Proc. Natl. Acad. Sci. USA 102, 15545–15550. [PubMed: 16199517]

Tusher VG, Tibshirani R, and Chu G (2001). Significance analysis of micro-arrays applied to the ionizing radiation response. Proc. Natl. Acad. Sci. USA 98, 5116–5121. [PubMed: 11309499]

Van't Veer LJ, Dai H, Van De Vijver MJ, He YD, Hart AA, Mao M, Peterse HL, Van Der Kooy K, Marton MJ, and Witteveen AT (2002). Gene expression profiling predicts clinical outcome of breast cancer. Nature 415, 530–536. [PubMed: 11823860]

Wagner KU, Wall RJ, St-Onge L, Gruss P, Wynshaw-Boris A, Garrett L, Li M, Furth PA, and Hennighausen L (1997). Cre-mediated gene deletion in the mammary gland. Nucleic Acids Res 25, 4323–4330. [PubMed: 9336464]

Weigelt B, Geyer FC, Natrajan R, Lopez-Garcia MA, Ahmad AS, Savage K, Kreike B, and Reis-Filho JS (2010a). The molecular underpinning of lobular histological growth pattern: a genome-wide transcriptomic analysis of invasive lobular carcinomas and grade-and molecular subtype-matched invasive ductal carcinomas of no special type. J. Pathol 220, 45–57. [PubMed: 19877120]

Weigelt B, Geyer FC, and Reis-Filho JS (2010b). Histological types of breast cancer: how special are they? Mol. Oncol 4, 192–208. [PubMed: 20452298]

Xu K, Usary J, Kousis PC, Prat A, Wang DY, Adams JR, Wang W, Loch AJ, Deng T, Zhao W, et al. (2012a). Lunatic fringe deficiency cooperates with the Met/Caveolin gene amplicon to induce basal-like breast cancer. Cancer Cell 21, 626–641. [PubMed: 22624713]

Xu X, Zhou Y, Xie C, Wei S-M, Gan H, He S, Wang F, Xu L, Lu J, Dai W, et al. (2012b). Genome-wide screening reveals an EMT molecular network mediated by Sonic hedgehog-Gli1 signaling in pancreatic cancer cells. PLoS ONE 7, e43119. [PubMed: 22900095]

Yu YR, O'Koren EG, Hotten DF, Kan MJ, Kopin D, Nelson ER, Que L, and Gunn MD (2016). A protocol for the comprehensive flow cytometric analysis of immune cells in normal and inflamed murine non-lymphoid tissues. PLoS ONE 11, e0150606. [PubMed: 26938654]

Zappasodi R, Budhu S, Hellmann MD, Postow MA, Senbabaoglu Y, Manne S, Gasmi B, Liu C, Zhong H, Li Y, et al. (2018). Non-conventional inhibitory CD4(+)Foxp3(−)PD-1(hi) T cells as a biomarker of immune checkpoint blockade activity. Cancer Cell 33, 1017–1032.e7. [PubMed: 29894689]

Zhao L, and Vogt PK (2010). Hot-spot mutations in p110alpha of phosphatidylinositol 3-kinase (pI3K): differential interactions with the regulatory subunit p85 and with RAS. Cell Cycle 9, 596–600. [PubMed: 20009532]

Highlights

- Development of mouse model for lobular BC with deletion of *Cdh1* and *Pik3ca* activation

- Mouse model shows gene expression signature akin to human immune-related lobular tumors

- Tumors show enhanced Rac and Yap signaling, with tumorsphere sensitivity to inhibitors

- Immune suppression and exhaustion in mouse model linked to myeloid and T cell anomalies
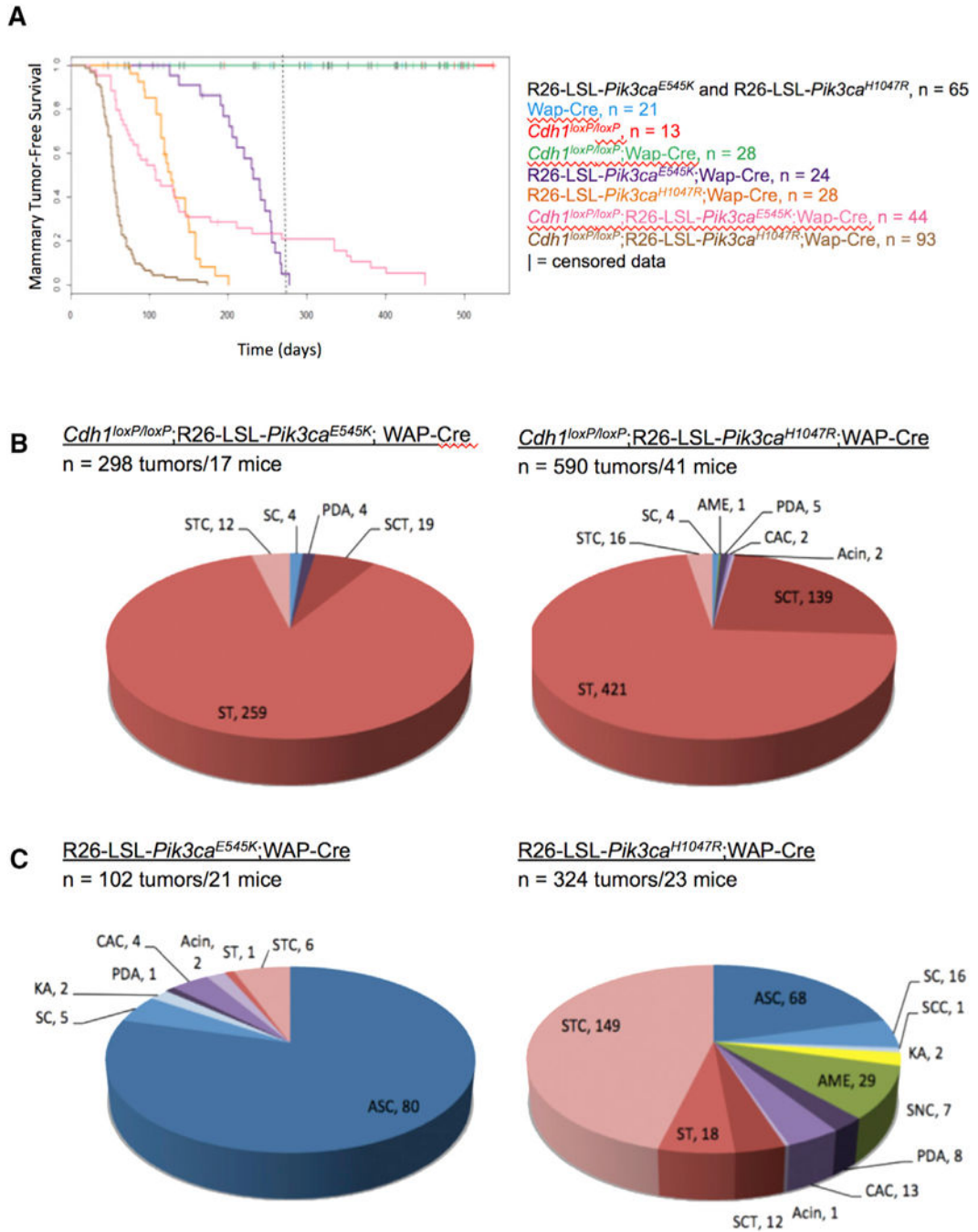
Figure 1. *Cdh1* and *Pik3ca* Mutations Cooperate to Induce Mammary Tumor Formation in Mice

(A) Kaplan-Meier mammary tumor-free survival curves show mammary tumor latency in cohorts of mice with mammary-specific deletion of *Cdh1* and expression of activated *Pik3ca* (*Pik3ca^E545K* and *Pik3ca^H1047R*) compared with mice with either mutation or other controls. A dashed line is included to highlight the date at which mammary tumor-free survival lines cross for mice from *Pik3ca*^E545K cohorts ± *Cdh1* homozygous deletion.

(B)Pie chart representation of mammary tumor pathology in female mice from *Cdh1*^{loxP/loxP};R26-LSL-*Pik3ca*^{E545K};WAP-Cre and *Cdh1*^{loxP/loxP};R26-LSL-*Pik3ca*^{H1047R};WAP-Cre cohorts.

(C) Pie chart representation of mammary tumor pathology in female mice from R26-LSL-*Pik3ca*^{E545K}; WAP-Cre and R26-LSL-*Pik3ca*^{E545K};WAP-Cre cohorts.

Acin, acinar adenocarcinoma; AME, adenomyoepithelioma; ASC, adenosquamous carcinoma; CAC, complex adenocarcinoma; KA, keratoacanthoma; PDA, poorly differentiated adenocarcinoma; RS, radial scar; SC, squamous cyst; SCC, squamous cell carcinoma; SCT, spindle cell tumor; SNC, solid nodular carcinoma; ST, scirrhous tumor; STC, scirrhous tubular carcinoma.
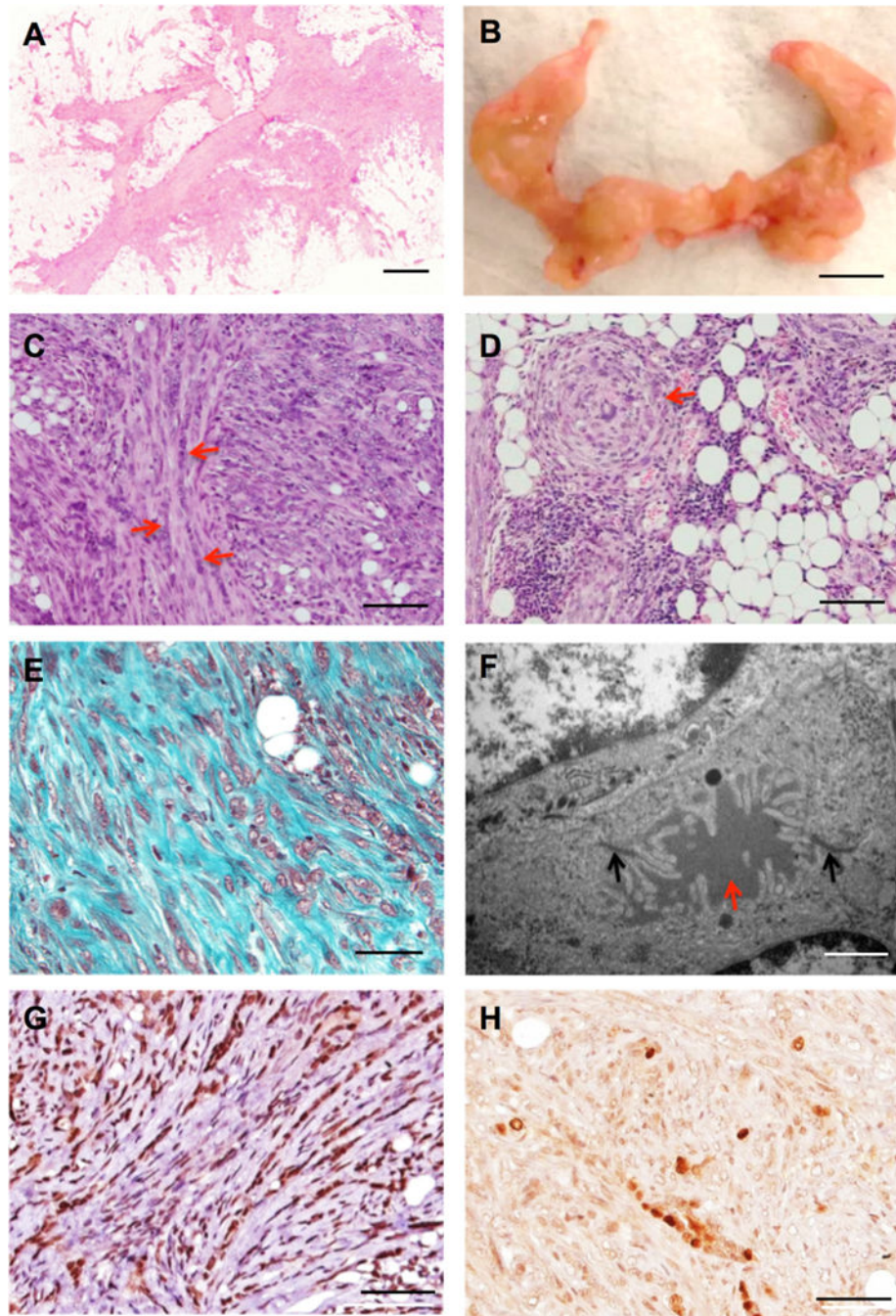
Figure 2. *Cdh1*^{loxP/loxP};*Pik3ca*^{mut} Mammary Tumors Share Morphological Features with Human ILC

(A) *Cdh1*^{loxP/loxP};*Pik3ca*^{H1047R} mouse tumor with diffusely infiltrative borders.

(B) *Cdh1*^{loxP/loxP};*Pik3caH1047R* tumor network connecting mammary glands 4 and 5 on each side of the midline.

(C) *Cdh1*^{loxP/loxP};*Pik3ca*^{H1047R} mammary tumor with ILC-like single-file invasive growth pattern (red arrows).

(D) Mouse tumor with targetoid growth (red arrows).

(E) Masson trichrome staining reveals an abundance of collagen between rows of tumor cells.

(F) Electron microscopy shows a small apical lumen between tumor cells (red arrow) with adjacent junctional complexes (black arrows).

(G and H) *Cdh1$^{loxP/loxP}$;R26-Pik3ca^{H1047R}* tumors express the estrogen receptor (G) and progester-one receptor (H).

See also Figure S2. Scale bars, 500, 5, 50, 50, 50, 1, 50, and 50 mm for (A)–(H), respectively.
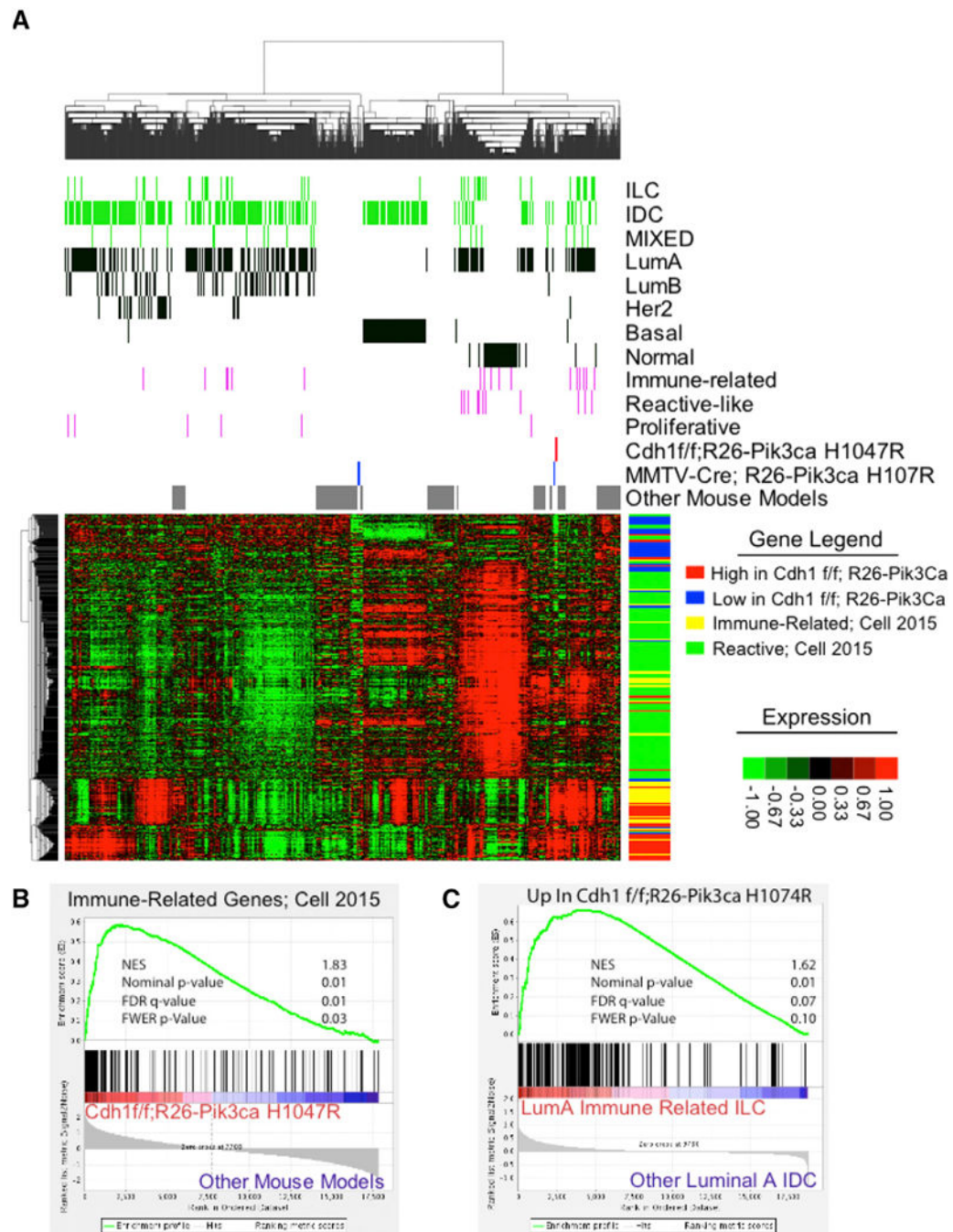
A

B Immune-Related Genes; Cell 2015

NES	1.83
Nominal p-value	0.01
FDR q-value	0.01
FWER p-Value	0.03

Cdh1f/f;R26-Pik3ca H1047R

Other Mouse Models

C Up In Cdh1 f/f;R26-Pik3ca H1074R

NES	1.62
Nominal p-value	0.01
FDR q-value	0.07
FWER p-Value	0.10

LumA Immune Related ILC

Other Luminal A IDC

Figure 3. Relationship of *Cdh1*$^{loxP/loxP}$;R26-*Pik3ca*^{H1047R} Tumors to Human Breast Cancer
(A) The dendrogram at the top illustrates relationships between human and mouse tumor samples. All human samples are from a TCGA (The Cancer Genome Atlas) cohort that includes invasive ductal carcinoma (IDC) from all major subtypes as well as ILC (Ciriello et al., 2015). This collection includes tumors from each intrinsic subtype. All mouse samples are from Pfefferle et al. (2013), plus the ten ILC-like samples described in this paper. Immediately below, color bars mark the position of each tumor type in the dendrogram and in the heatmap. Green bars mark the pathology, and black bars mark the intrinsic subtype of

human tumors. The magenta bars mark the ILC-subtype calls (Ciriello et al., 2015). The heatmap displays the median centered expression level (log$_2$) of each gene in a given sample; expression levels are depicted by the color bar on the right-hand side. On the right hand side of the heatmap, the color bar marks individual gene annotations for presence in a given signature.

(B) Gene set enrichment analysis comparing *Cdh1$^{loxP/loxP}$;R26-Pik3ca^{H1047R}* tumors with all other mouse mammary tumors reveals significant enrichment of the immune-related ILC signature (Ciriello et al., 2015) (normalized enrichment score = 1.83, nominal p value = 0.01, false discovery rate [FDR] q value = 0.01, family-wise error rate [FWER] p value = 0.03).

(C) Gene set enrichment analysis comparing immune-related ILC tumors that clustered with mouse *Cdh1$^{loxP/loxP}$;R26-Pik3ca^{H1047R}* tumors with all other luminal A IDC tumors reveals significant enrichment of the genes that were upregulated in mouse *Cdh1$^{loxP/loxP}$;R26-Pik3ca^{H1047R}* tumors (normalized enrichment score = 1.62, nominal p value = 0.01, FDR q value = 0.07, FWER p value = 0.1).
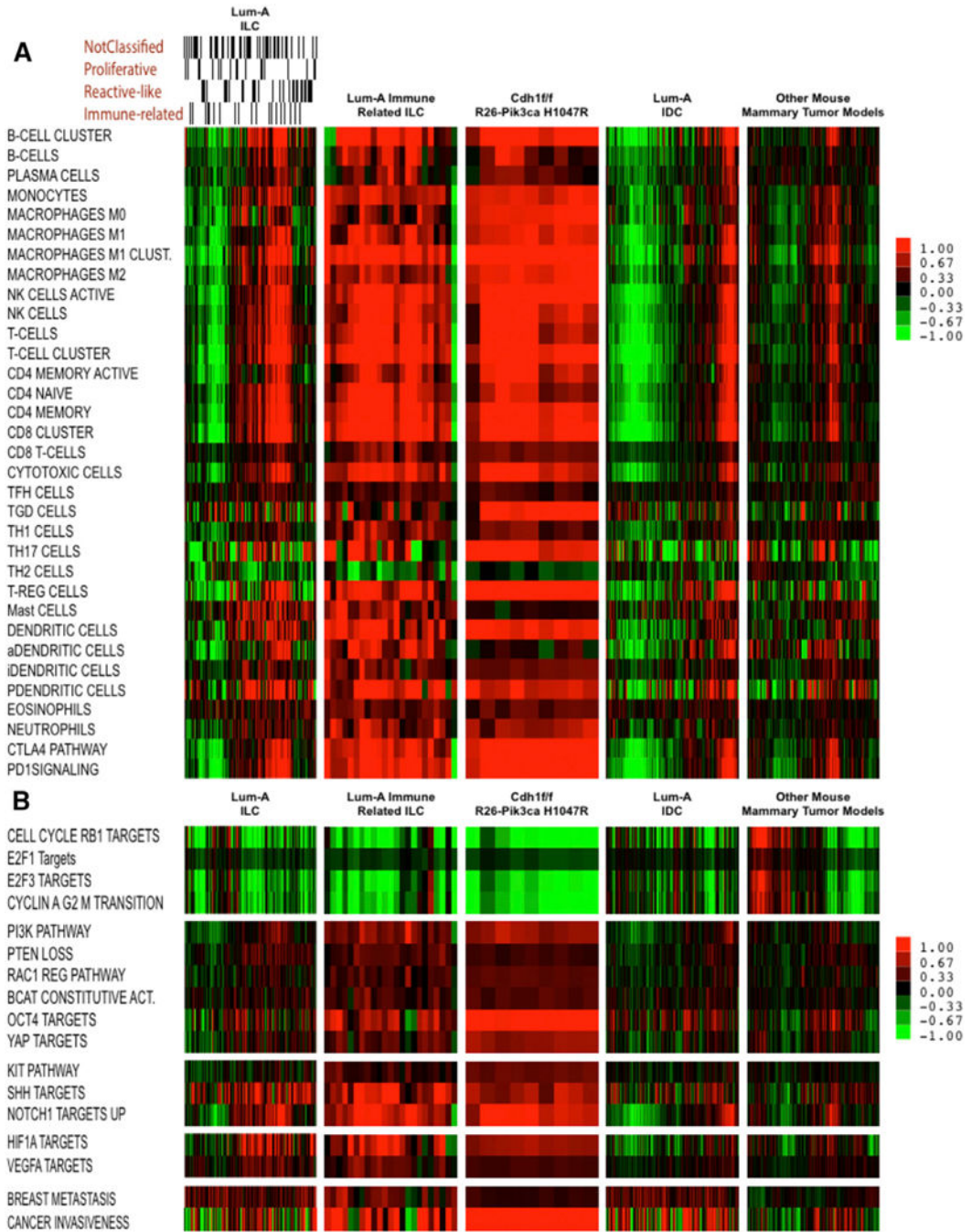
Figure 4. Shared Elevation of Immune and Pathway Signatures in *Cdh1*^loxP/loxP^;*R26-Pik3ca*^H1047R^ Tumors and Luminal A ILC Tumors

(A) The heatmap displays the expression of published gene expression signatures for immune cell types. Signature expression is displayed as the median expression of all genes within a signature for each sample according to the color bar on the right.

(B) The heatmap displays the expression of published pathway signatures for each tumor type. Tumors are grouped according to their tumor classification, with the immune-related group containing those that co-clustered with the murine *Cdh1* mutant tumors. Within each class, samples are ordered on the basis of centroid linkage for the signatures shown in both

panels. Importantly, sample ordering in (A) is preserved in (B). Signatures were obtained from the Broad Institute's molecular signature database (Subramanian et al., 2005; Liberzon et al., 2011).
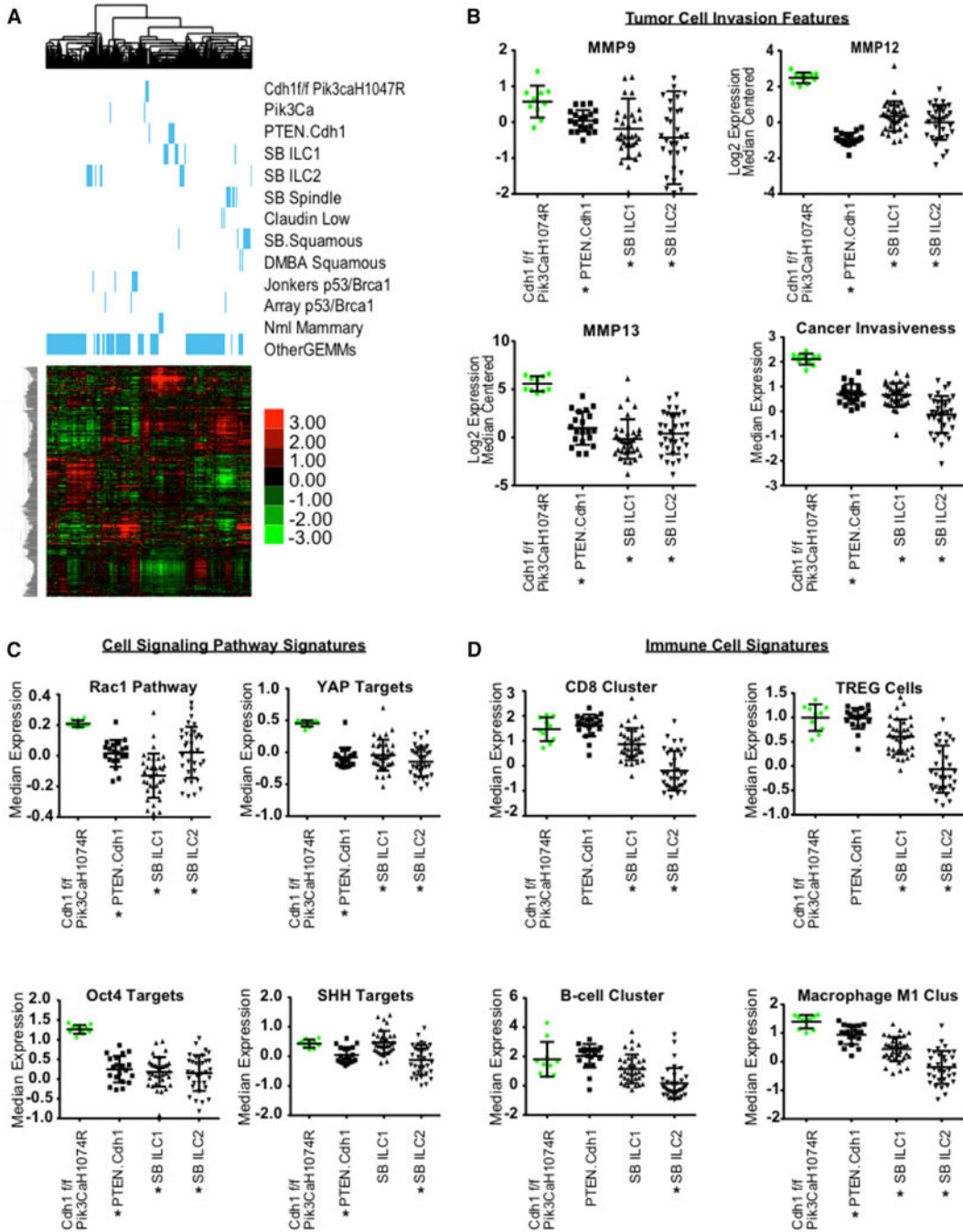
Figure 5. Comparative Analysis of Mouse Models for ILC

(A) Hierarchical clustering of our domestic dataset with imported data from PRJEB14134 and PRJEB14147 following batch correction. Genes were filtered to include only intrinsic gene sets and the dendrogram assembled by centroid linkage. Beneath the dendrogram, blue bars depict the position of tumors according to row annotations.

(B) Plots show expression levels for genes and signatures associated with tumor cell invasion (*p < 0.05).

(C) Plots show expression levels for cell signaling pathway signatures (*p < 0.05).

(D) Plots show expression levels for immune cell signatures (*p < 0.05). Bars depict the average and the SD in both directions.
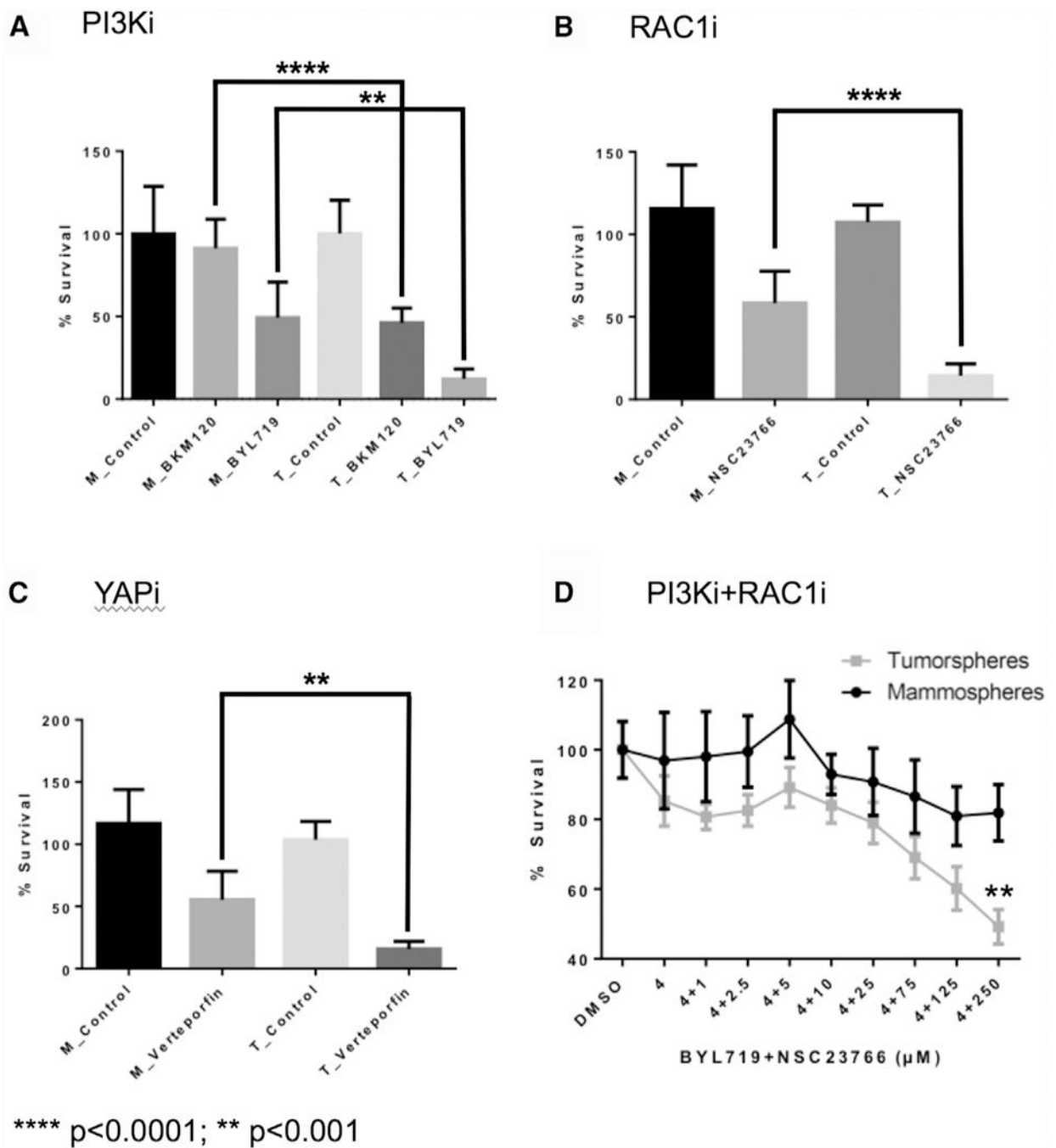
Figure 6. mILC Tumorspheres Are Sensitive to Inhibition of PI3K, Rac1, and Yap Signaling

(A) Sensitivity of normal mouse mammospheres (n = 3, in triplicate, where n represents the number of cell lines from independent animals) and mILC tumorspheres (n = 3, in triplicate) to the pan-PI3K inhibitor buparlisib (BKM120) (5 μM) and PI3Kα inhibitor alpelisib (BYL719) (8 μM).

(B) Sensitivity of normal mouse mammospheres (n = 3, in triplicate) and mILC tumorspheres (n = 3, in triplicate) to Rac1 inhibitor (NSC23766) (250 μM).

(C) Sensitivity of normal mouse mammospheres (n = 3, in triplicate) and mILC tumorspheres (n = 3, in triplicate) to the YAP inhibitor verteporfin (5 μg/mL).

(D) Sensitivity of normal mouse mammospheres (n = 3, in triplicate) and mILC tumorspheres (n = 3, in triplicate) to combined treatment with BYL719 and NSC23766. Bars depict the average and the SD above the average (A–C) or in both directions (D).
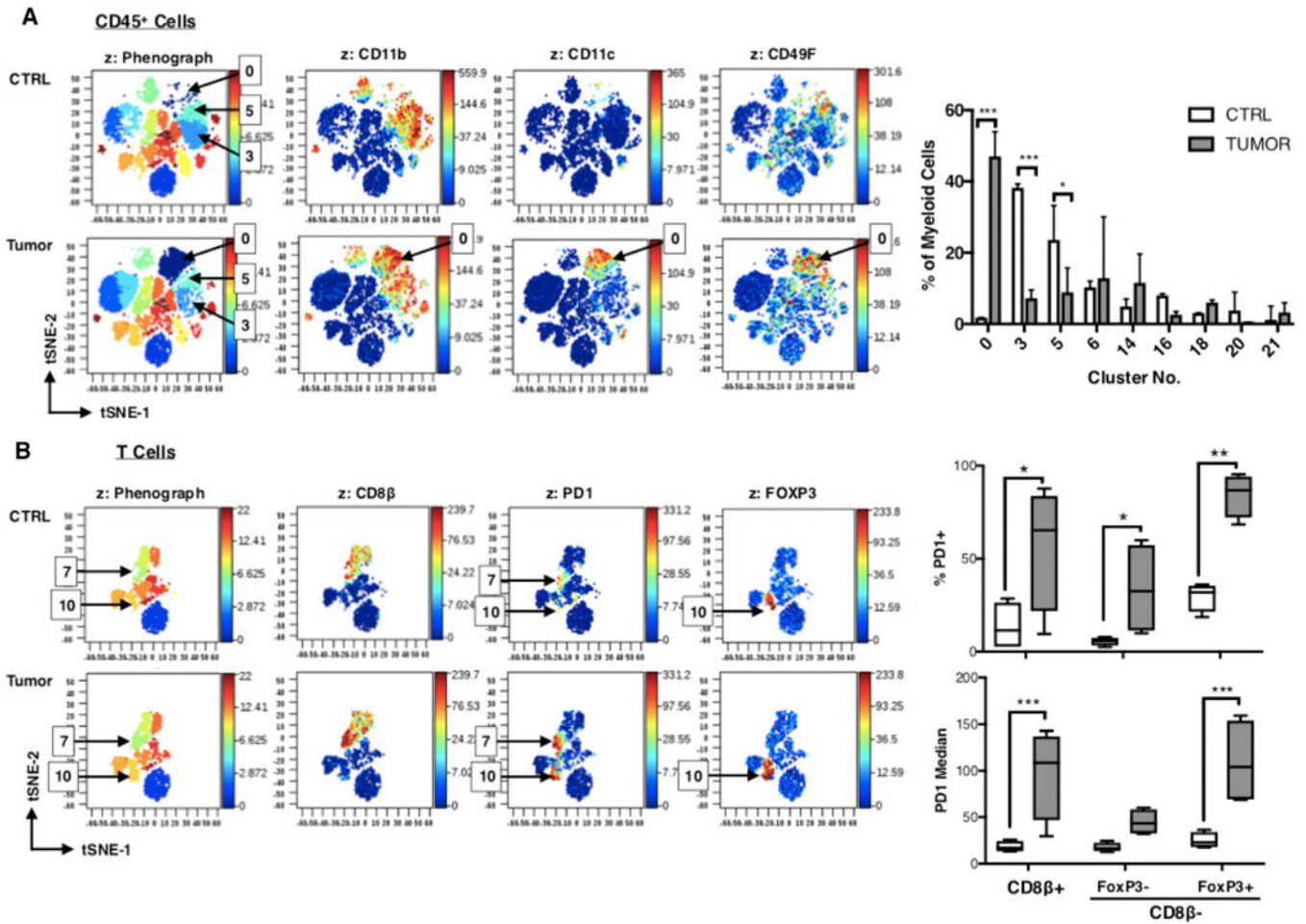
Figure 7. Identification of Immune Cell Subsets and Differentiation States in ILC

(A) Left: representative t-SNE plots of CD45^{+} cells present in enzymatically dissociated mammary gland (MG) from a control (CTRL) (top) versus tumor (bottom) mouse. Maps were colored in the z dimension by Phenograph cluster number (left) or the indicated myeloid markers. Right: bar graphs show the median (percentage) of each CD11b^{+} cluster among total myeloid cells. Vertical lines extending above each bar showing the range of values observed for each cluster. Arrows point to clusters that showed significantly different relative abundance between genotypes by multiple t testing, using a false discovery framework (FDR) of 5% to yield adjusted p values, referred to as q values. Significant differences are noted as follows: $*q < 0.05$, $**q < 0.005$, and $***q < 0.0005$. Clusters not marked with asterisks were not differentially abundant between genotypes.

(B) Left: representative t-SNE plots of CD3^{+} T cells in the same MG samples shown in (A), colored in the z dimension by Phenograph cluster number or the indicated T cell markers. Right: box-and-whisker plots show the percentage of PD1^{+} cells (top) or the median PD1 intensity among PD1^{+} cells (bottom) identified manually within the CD8b^{+}, CD8b FoxP3 and CD8b FoxP3^{+} regulatory T subsets (n = 4/group). Means are identified with a horizontal line on each bar, and whiskers show 10th to 90th percentile values. Asterisks denote significant FDR-adjusted q values as described for (A).